IEEE Open Journal of Antennas and Propagation

Received XX Month, XXXX; revised XX Month, XXXX; accepted XX Month, XXXX; Date of publication XX Month, XXXX; date of current version XX Month, XXXX.

Digital Object Identifier 10.1109/OJAP.2020.1234567

Nyström-type Technique for Electromagnetic Wave Scattering in Inhomogeneous Material, Plasma and Metamaterial Slabs

John L. Tsalamengas

[1]School of Electrical and Computer Engineering, National Technical University of Athens, GR-15773 Zografou, Athens, Greece

CORRESPONDING AUTHOR: John L. Tsalamengas (e-mail: itsal@central.ntua.gr).

ABSTRACT We present a simple, stable, and spectrally-accurate quasi-analytical method for studying the reflection, transmission, and radiation of EM waves in the presence of single-layer or multilayer material, plasma, or metamaterial slabs that are inhomogeneous along the normal to the slab interfaces. Our approach formulates the problem as a linear Volterra integral equation of the second kind, discretized using an entire-domain Nyström method with a high-order Gauss-type quadrature. The proposed algorithms ensure mathematically guaranteed spectral convergence, handle electrically thin to electrically thick slabs, and can accommodate discontinuous inhomogeneity profiles. Application examples include one-dimensional band-gap structures, field enhancement in inhomogeneous metamaterial slabs with zero-crossings in permittivity, and dipole-driven plasma antennas.

INDEX TERMS Dipole antennas, electromagnetic (EM) bandgap materials, EM scattering by nonhomogeneous media, EM scattering by plasma media, nonhomogeneous media, Volterra integral equations, Nyström method.

I. INTRODUCTION

INHOMOGENEOUS planar layers have diverse applications in integrated optics, photonics, plasma, and microwave engineering [1]–[7]. Graded-index slabs, for instance, are used for optical waveguide design and the creation of optical components. Slabs with periodically modulated refractive indices exhibit frequency-selective behaviour, serving as simple one-dimensional EM band-gap structures. Inhomogeneous plasma layers are employed in radio communications, radio astronomy, and stealth applications due to their adaptable reflection, absorption, and transmission characteristics. Other significant applications include geophysical exploration, biomedical imaging, and optical tomography.

Analyzing wave propagation in infinite inhomogeneous slabs almost always relies on approximation methods because exact solutions are seldom available for arbitrary material parameter distributions. The most common approach is the staircase approximation (SA), which models the inhomogeneous slab as a stack of thin homogeneous layers and then applies matrix propagation methods [8]–[11]. While SA is simple, it requires a thin stratification for accurate results and exhibits low convergence. Another widely used approach involves converting the generalized Helmholtz equation into a Riccati (nonlinear) differential equation for the local reflection coefficient and solving it as an initial value problem using the Runge-Kutta method [12], [13]. Several alternative approaches, such as series-expansion [14]–[16], integral equations [17]–[19], and others [20]–[25], are also available.

A distinct quasi-analytical method, which combines differential and integral equation techniques and exhibits spectral convergence, has recently been used to investigate EM scattering from inhomogeneous isotropic or anisotropic cylindrical [26], [27] or spherical [28] objects. In this study, we extend the application of this method to address scattering by single and multilayered slabs made of materials, plasma, or metamaterials exhibiting inhomogeneity along the normal to the slab interfaces. We consider two types of incident fields: plane waves and spherical waves radiated by elementary dipoles. Inhomogeneity profiles can be smooth or piecewise smooth spatial functions. Our primary goal is a simple, stable, and spectrally accurate algorithm that can provide machine-precision results. We will approach this in two steps.

This work is licensed under a Creative Commons Attribution 4.0 License. For more information, see https://creativecommons.org/licenses/by/4.0/

We start by reformulating Maxwell's equations in the region occupied by the slab as a first-order system of ordinary differential equations (ODEs) with a spatially-varying coefficient matrix (Sections II-IV). When addressing the associated initial value problem (IVP), a variety of efficient and reliable numerical schemes are available, typically divided into linear multistep and Runge-Kutta methods. However, selecting the optimal scheme can be a complex task due to the trade-offs between stability, convergence properties, computational complexity, and memory usage. Additionally, these methods are limited by their algebraic order of accuracy and tend to degrade in performance when faced with discontinuous inhomogeneity profiles.

Recognizing these limitations, we depart from the conventional numerical schemes commonly associated with IVPs in the second step. Instead, we transform the system of ODEs into an equivalent linear Volterra integral equation (VIE) of the second kind. The transformation is followed (Section V) by discretization of the resulting VIE using a specialized high-order entire-domain Nyström method, coupled with an appropriate Gauss-type quadrature.

The proposed algorithms ensure mathematically guaranteed spectral convergence, constrained only by the smoothness of the underlying inhomogeneity profiles. When dealing with analytic spatial functions, the convergence is exponential. This stands in contrast to widely used general-purpose methods that exhibit an algebraic convergence rate of $\mathcal{O}(h^p)$; in such methods, the convergence rate is determined by the order p regardless of the regularity of the underlying function. Additionally, our algorithms provide simple closed-form expressions for every entry of the Nyström matrix, apply across a wide range of slab thicknesses, and can efficiently handle profile discontinuities. As a result, we attain machine-precision results at low computational and implementation costs.

Throughout this work, we assume a time-harmonic dependence of $\exp(i\omega t)$, which we omit for brevity.

II. SCATTERING OF E-POLARIZED PLANE WAVES

Fig. 1 shows an inhomogeneous slab, region 1, with thickness d and continuous constitutive parameters $\varepsilon_1(z) = \varepsilon_0\varepsilon_{r1}(z)$ and $\mu_1(z) = \mu_0\mu_{r1}(z)$. Sectionally continuous parameters will be addressed in Section VI. The slab extends infinitely in the x and y directions, surrounded by homogeneous regions 0 ($z > z_1 = 0$) and 2 ($z < z_0 = -d$) with constitutive parameters (ε_0, μ_0) and (ε_2, μ_2), respectively. Both (ε_1, μ_1) in region 1 and (ε_2, μ_2) in region 2 can be complex to account for potential losses. The primary excitation is an incident E-polarized plane EM wave propagating in the direction of $\bar{k}^{inc} = -k_x\hat{x} - k_z\hat{z}$, where

$$k_x = k_0 \sin\psi,\ k_z = k_0 \cos\psi. \tag{1}$$

In (1), $k_0 = \omega\sqrt{\varepsilon_0\mu_0}$, and ψ is the incidence angle measured from the z-axis, increasing clockwise. The electric field, with an amplitude of E_0, is given by

$$\bar{E}^{inc}(x,z) = \hat{y}E_0 e^{i(k_x x + k_z z)}.$$

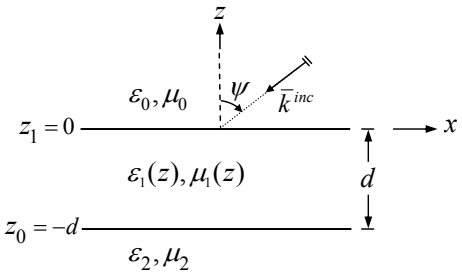

FIGURE 1. Geometry of an inhomogeneous slab.

Remark 1. In each region, the field components vary as $f(z)e^{ik_x x}$, with the phase factor $\exp(ik_x x)$ dictated by the incident wave. □

In regions 0 and 2, the nonzero component of the total electric field is expressed as

$$E_{y0}(x,z) = E_y^{inc}(x,z) + E_0\mathtt{R}\, e^{i(k_x x - k_z z)} \tag{2a}$$

$$E_{y2}(x,z) = E_0\mathtt{T}\, e^{i(k_x x + k_{z2} z)}, \tag{2b}$$

where R and T are the reflection and transmission coefficients, respectively. In (2b), $k_{z2} = \sqrt{k_2^2 - k_x^2}$ with $k_2 = \omega\sqrt{\varepsilon_2\mu_2}$. For a lossy medium in region 2, $k_2^2 - k_x^2$ falls within the lower half-plane of the complex plane. To ensure a physically valid solution, we choose the branch of the square root defining k_{z2} in such a way that $\mathrm{Re}(k_{z2}) \geq 0$ and $\mathrm{Im}(k_{z2}) \leq 0$. The components of the associated magnetic field are obtained from

$$H_x = \frac{1}{i\omega\mu}\frac{\partial E_y}{\partial z}, \quad H_z = -\frac{1}{i\omega\mu}\frac{\partial E_y}{\partial x} \tag{3}$$

with $\mu = \mu_0$ or $\mu = \mu_2$.

For the field in region 1, with components $F(x,z) = e^{ik_x x}\tilde{F}(z)$ ($F = E_{y1}, H_{x1}, H_{z1}$), from Maxwell's equations we obtain an algebraic equation:

$$H_{z1}(z) = \frac{k_x}{\omega\mu_1(z)}E_{y1}(z) \tag{4}$$

and an ODE:

$$\frac{d\bar{u}(z)}{dz} = A_1(z)\bar{u}(z), \tag{5}$$

where the column-vector variable $u(z)$ is defined as

$$\bar{u}(z) = [\tilde{E}_{y1}(z), \tilde{H}_{x1}(z)]^{\mathsf{T}} \tag{6}$$

and the matrix $A_1(z)$ is given by

$$A_1(z) = A_1(z;\varepsilon_1,\mu_1) = \begin{bmatrix} 0 & i\omega\mu_1(z) \\ \frac{k_x^2 - k_1^2(z)}{i\omega\mu_1(z)} & 0 \end{bmatrix} \tag{7}$$

with $k_1^2(z) = \omega^2\varepsilon_1(z)\mu_1(z)$.

A. SOLUTION OUTLINE

The general solution of (5) is:

$$\bar{u}(z) = W_1(z, z_0)\bar{u}(z_0), \quad z_0 \le z \le z_1, \tag{8}$$

where $W_1(z, z_0)$ is the transition matrix associated with the system matrix $A_1(z)$. The transition matrix is the solution of the matrix-valued IVP:

$$\frac{dW_1(z, z_0)}{dz} = A_1(z)W_1(z, z_0), \quad W_1(z_0, z_0) = I_2, \tag{9}$$

where I_2 denotes the 2×2 identity matrix.

The highly accurate computation of $W_1(z, z_0)$, carried out in Section V, is an integral part of our method. After obtaining $W_1(z_1, z_0)$, we enforce continuity on $\bar{u}(z)$ at $z = z_0$ and $z = z_1$, leading to:

$$E_{0\mathtt{T}} e^{ik_{z2}z_0} \begin{bmatrix} 1 \\ \frac{k_{z2}}{\omega\mu_2} \end{bmatrix} = \bar{u}(z_0), \quad \Lambda \cdot \bar{h} = \begin{bmatrix} 1 \\ \frac{k_z}{\omega\mu_0} \end{bmatrix}, \tag{10}$$

where

$$\bar{h} = \begin{bmatrix} Re^{-i2k_z z_1} \\ Te^{-i(k_z z_1 - k_{z2} z_0)} \end{bmatrix}, \tag{11}$$

and Λ is the 2×2 block matrix:

$$\Lambda = \left[\begin{pmatrix} -1 \\ \frac{k_z}{\omega\mu_0} \end{pmatrix} \;\middle|\; W_1(z_1, z_0) \begin{pmatrix} 1 \\ \frac{k_{z2}}{\omega\mu_2} \end{pmatrix} \right]. \tag{12}$$

Once we obtain the unknowns $\mathtt{R}$, $\mathtt{T}$, and $\bar{u}(z_0)$ from (10), we can evaluate the field everywhere using (2)-(4) and (8).

B. DNG SLABS

Our analysis extends to arbitrary isotropic inhomogeneous materials or metamaterial slabs. Assuming all media are lossless, we apply the second equation in (10) to a double-positive (DPS) slab with $\varepsilon_1(z) > 0$ and $\mu_1(z) > 0$. We then apply the same equation to its double-negative (DNG) counterpart with $-\varepsilon_1(z)$ and $-\mu_1(z)$. This yields:

$$\Lambda^{\text{DPS}} \cdot \bar{h}^{\text{DPS}} = \Lambda^{\text{DNG}} \cdot \bar{h}^{\text{DNG}} = (\Lambda^{\text{DNG}} \cdot \bar{h}^{\text{DNG}})^* \equiv \begin{bmatrix} 1 \\ \frac{k_z}{\omega\mu_0} \end{bmatrix},$$

where the star (*) denotes the complex conjugate. Clearly, $A_1^*(z; -\varepsilon_1, -\mu_1) = A_1(z; \varepsilon_1, \mu_1)$, implying $(W_1^{\text{DNG}})^* = W_1^{\text{DPS}}$ so that $(\Lambda^{\text{DNG}})^* = \Lambda^{\text{DPS}}$. Thus, $\bar{h}^{\text{DPS}} = (\bar{h}^{\text{DNG}})^*$ by (10). With $z_1 = 0$ and $z_0 = -d$, as in Fig. 1, we obtain:

$$(R, T)^{\text{DNG}} = (R^*, e^{2ik_{z2}d}T^*)^{\text{DPS}}. \tag{13}$$

Hence, the transition from a DPS slab to its DNG counterpart does not alter the reflectance ($|R|^2$) and transmittance ($|T|^2$).

III. SCATTERING OF H-POLARIZED PLANE WAVES

In this section, we investigate the dual problem to the previous one. The incident plane wave is now H-polarized, and its magnetic field is given by

$$\bar{H}^{inc}(x, z) = \hat{y}H_0 e^{i(k_x x + k_z z)}.$$

In regions 0 and 2, the nonzero component of the total magnetic field is expressed as

$$H_{y0}(x, z) = H_y^{inc}(x, z) + H_{0\mathtt{R}}\, e^{i(k_x x - k_z z)}, \tag{14}$$

$$H_{y2}(x, z) = H_{0\mathtt{T}}\, e^{i(k_x x + k_{z2} z)}, \tag{15}$$

where $\mathtt{R}$ and $\mathtt{T}$ are the reflection and transmission coefficients, respectively. The components of the associated electric field can be obtained from

$$E_x = -\frac{1}{i\omega\varepsilon}\frac{\partial H_y}{\partial z}, \quad E_z = \frac{1}{i\omega\varepsilon}\frac{\partial H_y}{\partial x} \tag{16}$$

with $\varepsilon = \varepsilon_0$ or ε_2.

For the field in region 1, with components $F(x, z) = e^{ik_x x}\tilde{F}(z)$ ($F = H_{y1}, E_{x1}, E_{z1}$), from Maxwell equations we obtain an algebraic equation:

$$E_{z1}(z) = \frac{k_x}{\omega\varepsilon_1(z)} H_{y1}(z) \tag{17}$$

and an ODE:

$$\frac{d\bar{v}(z)}{dz} = A_2(z)\bar{v}(z), \tag{18}$$

where the column-vector variable $v(z)$ is defined as

$$\bar{v}(z) = \left[\tilde{H}_{y1}(z), -\tilde{E}_{x1}(z)\right]^{\intercal}. \tag{19}$$

The matrix $A_2(z)$ is the dual of $A_1(z)$ and is given by

$$A_2(z) = \begin{bmatrix} 0 & i\omega\varepsilon_1(z) \\ \frac{k_x^2 - k_1^2(z)}{i\omega\varepsilon_1(z)} & 0 \end{bmatrix}. \tag{20}$$

The general solution of (18) is:

$$\bar{v}(z) = W_2(z, z_0)\bar{v}(z_0), \quad z_0 \le z \le z_1, \tag{21}$$

where $W_2(z, z_0)$ is the solution of the matrix-valued IVP:

$$\frac{dW_2(z, z_0)}{dz} = A_2(z)W_2(z, z_0), \quad W_2(z_0, z_0) = I_2. \tag{22}$$

The transition matrix W_2 can be computed as in Section V.

Enforcing continuity on the vector variable $\bar{v}(z)$ at $z = z_0$ and $z = z_1$, yields:

$$H_{0\mathtt{T}} e^{ik_{z2}z_0} \begin{bmatrix} 1 \\ \frac{k_{z2}}{\omega\varepsilon_2} \end{bmatrix} = \bar{v}(z_0),$$

$$\left[\begin{pmatrix} -1 \\ \frac{k_z}{\omega\mu_0} \end{pmatrix} \;\middle|\; W_2(z_1, z_0) \begin{pmatrix} 1 \\ \frac{k_{z2}}{\omega\mu_2} \end{pmatrix} \right] \cdot \bar{h} = \begin{bmatrix} 1 \\ \frac{k_z}{\omega\varepsilon_0} \end{bmatrix} \tag{23}$$

with $\bar{h}$ defined in (11). Equation (23) is the dual of (10). Once we obtain the unknowns $\mathtt{R}$, $\mathtt{T}$, and $\bar{v}(z_0)$ from (23), we can evaluate the field everywhere using (14)-(17) and (21).

Note: Property (13) is applicable in this case as well.

IV. ELECTRIC AND MAGNETIC DIPOLE RADIATION

In Sections IV.A and IV.B, we deal with arbitrarily oriented electric and magnetic dipoles

$$\bar{p} = p_x\hat{x} + p_y\hat{y} + p_z\hat{z}, \quad \bar{m} = m_x\hat{x} + m_y\hat{y} + m_z\hat{z},$$

located at $\bar{r}'(x', y', z')$ over a bilateral [Fig. 2(a)] or grounded [Fig. 2(b)] slab. Section IV.C focuses on dipoles embedded in either of these slabs, whereas Section IV.D concerns dipoles radiating in the presence of DNG slabs. For simplicity, we assume that region 2 ($z < z_0$) in the structure of Fig. 2(a) has the properties of vacuum (ε_0, μ_0). However, the analysis readily extends to include the general case where a homogeneous medium (ε_2, μ_2) occupies that region.

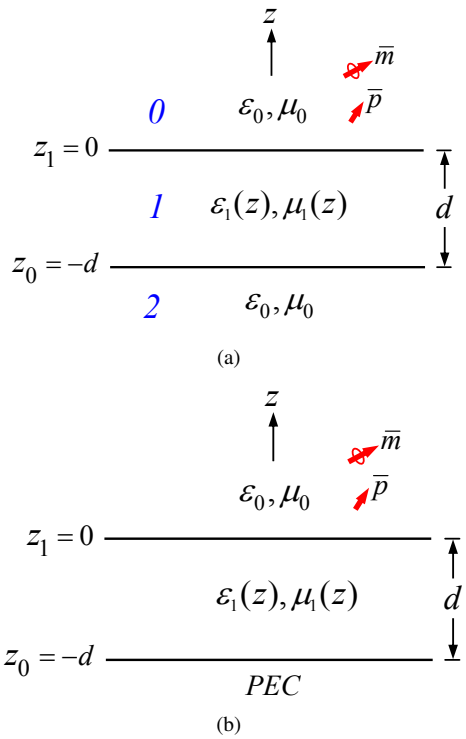

FIGURE 2. (a) Bilateral inhomogeneous slab excited by an arbitrarily oriented elementary electric or magnetic dipole. (b) Grounded inhomogeneous slab.

A. DIPOLES ON TOP OF AN INHOMOGENEOUS SLAB

We start with the problem of electric and magnetic dipoles radiating on top of the inhomogeneous slab of Fig. 2(a).

1) Field Representation Inside the Slab

In the 2D Fourier-transform domain defined by the pair:

$$f(x,y,z) = \iint_{-\infty}^{+\infty} e^{-i(k_x x + k_y y)}\, \tilde{f}(k_x,k_y;z)\, dk_x\, dk_y, \quad (24a)$$

$$\tilde{f}(k_x,k_y;z) = \frac{1}{(2\pi)^2} \iint_{-\infty}^{+\infty} e^{i(k_x x + k_y y)}\, f(x,y,z)\, dx\, dy, \quad (24b)$$

Maxwell's equations for region 1 split into two algebraic equations:

$$k_x\tilde{E}_{y1} - k_y\tilde{E}_{x1} = \omega\mu_1\tilde{H}_{z1},\ -k_x\tilde{H}_{y1} + k_y\tilde{H}_{x1} = \omega\varepsilon_1\tilde{E}_{z1},$$

together with four first-order scalar differential equations having the components of the column-vector variable

$$\bar{u}_1(z) = \left[\tilde{E}_{x1}(z), \tilde{E}_{y1}(z), \tilde{H}_{x1}(z), \tilde{H}_{y1}(z)\right]^{\mathsf{T}} \quad (25)$$

as the unknowns. Here, for simplicity, we use $\tilde{f}_{q1}(z)$ as shorthand for $\tilde{f}_{q1}(k_x,k_y;z)$, where f can be either E or H, and q can be either x or y. Let

$$L = \begin{bmatrix} k_x & k_y \\ k_y & -k_x \end{bmatrix}, \quad \bar{w}_1(z) = \begin{bmatrix} L & 0 \\ 0 & L \end{bmatrix} \bar{u}_1(z). \quad (26)$$

After suitable manipulation, we obtain the following ODE:

$$\frac{d\bar{w}_1(z)}{dz} = A_3(z)\bar{w}_1(z), \quad (27)$$

where

$$A_3(z) = i\begin{bmatrix} 0 & 0 & 0 & \frac{-\gamma_1^2(z)}{\omega\varepsilon_1(z)} \\ 0 & 0 & -\omega\mu_1(z) & 0 \\ 0 & \frac{\gamma_1^2(z)}{\omega\mu_1(z)} & 0 & 0 \\ \omega\varepsilon_1(z) & 0 & 0 & 0 \end{bmatrix} \quad (28)$$

with

$$\gamma_1^2(z) = k_x^2 + k_y^2 - \omega^2\varepsilon_1(z)\mu_1(z). \quad (29)$$

The general solution of (27) is:

$$\bar{w}_1(z) = W_3(z,z_0)\bar{w}_1(z_0), \quad z_0 \le z \le z_1, \quad (30)$$

where $W_3(z,z_0)$, the transition matrix of the linear differential system (27), satisfies the IVP:

$$\frac{dW_3(z,z_0)}{dz} = A_3(z)W_3(z,z_0), \quad W_3(z_0,z_0) = I_4 \quad (31)$$

with I_4 denoting the 4×4 identity matrix. The computation of $W_3(z,z_0)$ is detailed in Section V. The term $\bar{w}_1(z_0)$ encountered in (30) is elaborated in Section IV.A.4.

Once $\bar{w}_1(z)$ is determined, we can evaluate $\bar{u}_1(z)$ using (26):

$$\bar{u}_1(z) = \frac{1}{\lambda^2}\begin{bmatrix} L & 0 \\ 0 & L \end{bmatrix} \bar{w}_1(z), \qquad \lambda^2 = k_x^2 + k_y^2. \quad (32)$$

2) Field Representation in Region 2

In the homogeneous source-free region 2, the field can be described using scalar electric (π_{e2}) and magnetic (π_{m2}) Hertz potentials [29]:

$$\bar{E}_2 = \nabla\times\nabla\times(\hat{y}\pi_{e2}) - i\omega\mu_0\nabla\times(\hat{y}\pi_{m2}), \quad (33)$$

$$\bar{H}_2 = \nabla\times\nabla\times(\hat{y}\pi_{m2}) + i\omega\varepsilon_0\nabla\times(\hat{y}\pi_{e2}). \quad (34)$$

Both π_{e2} and π_{m2} satisfy homogeneous Helmholtz equations:

$$\left(\nabla^2 + k_0^2\right)\pi_{q2}(x,y,z) = 0, \quad q = e,m \quad (35)$$

with Fourier-transform counterparts:

$$\left(\frac{d^2}{dz^2} + k_0^2 - \lambda^2\right)\tilde{\pi}_{q2}(k_x,k_y;z) = 0. \quad (36)$$

Using, for simplicity of notation, the shorthand $\tilde{\pi}_{q2}(z)$ for $\tilde{\pi}_{q2}(k_x,k_y;z)$, we obtain:

$$\tilde{\pi}_{e2}(z) = a_2 e^{\gamma(z-z_0)}, \quad \tilde{\pi}_{m2}(z) = b_2 e^{\gamma(z-z_0)}. \quad (37)$$

Here, $a_2 = a_2(k_x,k_y)$ and $b_2 = b_2(k_x,k_y)$ are coefficients to be determined, and

$$\gamma = \left(\lambda^2 - k_0^2\right)^{\frac{1}{2}}, \quad -\frac{\pi}{2} < \arg(\gamma) \le \frac{\pi}{2}. \quad (38)$$

Selecting the branch of the double-valued function γ as in (38), ensures the validity of the radiation condition at $z \to -\infty$.

We introduce the vector variable $\bar{w}_2(z)$, defined analogously to $\bar{w}_1(z)$ but with the index 1 replaced by 2 in both

(25) and (26). Combining (33) and (34) with (37), we express $\bar{w}_2(z)$ as:

$$\bar{w}_2(z) = C(\gamma)\begin{bmatrix} a_2 \\ b_2 \end{bmatrix} e^{\gamma(z-z_0)}, \tag{39}$$

where

$$C(\gamma) = \lambda^2 \begin{bmatrix} -i\gamma & 0 & 0 & \omega\varepsilon_0 \\ 0 & -\omega\mu_0 & -i\gamma & 0 \end{bmatrix}^{\mathsf{T}}. \tag{40}$$

Here, the superscript T denotes the transpose operation.

3) Field Representation in Region 0

The field in region 0 can be written as a sum of two components:

$$\begin{Bmatrix} \bar{E}_0(\bar{r}) \\ \bar{H}_0(\bar{r}) \end{Bmatrix} = \begin{Bmatrix} \bar{E}_d(\bar{r}) \\ \bar{H}_d(\bar{r}) \end{Bmatrix} + \begin{Bmatrix} \bar{E}_s(\bar{r}) \\ \bar{H}_s(\bar{r}) \end{Bmatrix}. \tag{41}$$

The first component, denoted by the subscript d, represents the primary field that would be generated by the dipole source radiating in an unbounded space with parameters (ε_0, μ_0). We introduce the vector variable $\bar{w}_d(z)$, defined similarly to $w_1(z)$ but with the index 1 replaced by d in both (25) and (26). It can be shown [29] that

$$\bar{w}_d(z) = g(k_x, k_y, z)\bar{c}_d, \tag{42}$$

where

$$g(k_x, k_y, z) = \frac{1}{8\pi^2} e^{ik_x x' + ik_y y' - \gamma|z-z'|} \tag{43}$$

and $\bar{c}_d$ is defined as follows:

- For the electric dipole case:

$$\bar{c}_d = \begin{bmatrix} \frac{i\gamma k_x}{\omega\varepsilon_0} & \frac{i\gamma k_y}{\omega\varepsilon_0} & \frac{s\lambda^2}{\omega\varepsilon_0} \\ -\frac{ik_0^2 k_y}{\omega\varepsilon_0\gamma} & \frac{ik_0^2 k_x}{\omega\varepsilon_0\gamma} & 0 \\ -k_y s & k_x s & 0 \\ k_x s & k_y s & -\frac{i\lambda^2}{\gamma} \end{bmatrix} \begin{bmatrix} p_x \\ p_y \\ p_z \end{bmatrix}. \tag{44}$$

Here, $s = \text{sign}(z - z')$.

- For the magnetic dipole case:

$$\bar{c}_d = \begin{bmatrix} k_y s & -k_x s & 0 \\ -k_x s & -k_y s & \frac{i\lambda^2}{\gamma} \\ \frac{i\gamma k_x}{\omega\mu_0} & \frac{i\gamma k_y}{\omega\mu_0} & \frac{s\lambda^2}{\omega\mu_0} \\ -\frac{ik_0^2 k_y}{\omega\mu_0\gamma} & \frac{ik_0^2 k_x}{\omega\mu_0\gamma} & 0 \end{bmatrix} \begin{bmatrix} m_x \\ m_y \\ m_z \end{bmatrix}. \tag{45}$$

The second component, denoted by the subscript s, represents the secondary field, also known as the scattered field. It satisfies the source-free Maxwell equations and can be expressed in terms of two scalar Hertz potentials, π^s_{e0} and π^s_{m0}, using formulas similar to (33) and (34). The Fourier transforms $\tilde{\pi}^s_{e0}$ and $\tilde{\pi}^s_{m0}$ are given by

$$\tilde{\pi}^s_{e0}(z) = a_0 e^{-\gamma(z-z_1)}, \quad \tilde{\pi}^s_{m0}(z) = b_0 e^{-\gamma(z-z_1)}, \tag{46}$$

where $a_0 = a_0(k_x, k_y)$ and $b_0 = b_0(k_x, k_y)$ are unknown coefficients to be determined. Following a similar analysis as in Section IV.A.2, we arrive at

$$\bar{w}_s(z) = C(-\gamma)\begin{bmatrix} a_0 \\ b_0 \end{bmatrix} e^{-\gamma(z-z_1)}, \tag{47}$$

where $\bar{w}_s(z)$ is defined in a similar manner to $w_1(z)$, with the index 1 replaced by s in both (25) and (26).

4) Finalizing the Solution

To determine the yet-unknown coefficients $\{a_0, b_0, a_2, b_2\}$ and subsequently find the Fourier transforms of the fields, we impose continuity on both the electric and magnetic fields' x and y components—equivalent to enforcing continuity on $\bar{w}(z)$—at $z = z_0$ and $z = z_1$. Using (30), we obtain a 4×4 system of linear algebraic equations:

$$W_3(z_1, z_0)C(\gamma)\begin{bmatrix} a_2 \\ b_2 \end{bmatrix} - C(-\gamma)\begin{bmatrix} a_0 \\ b_0 \end{bmatrix} = \bar{w}_d(z_1). \tag{48}$$

Once these coefficients are determined, we can evaluate $\bar{w}_s(z)$ and $\bar{w}_2(z)$ using (47) and (39), respectively. Subsequently, we can obtain $\bar{w}_1(z)$ by using (30) with the condition $\bar{w}_1(z_0) = \bar{w}_2(z_0)$. The field can then be computed everywhere by applying the inverse Fourier transform (24a).

5) Far Field

In the radiation zone ($r \gg \lambda_0$), the generated field consists of two parts: a space wave component, representing the 3D radiation field in regions 0 and 2, and a surface wave component, characterizing the 2D waveguide modal field across all three regions. The evaluation of these field components can be carried out analytically via contour integration techniques detailed in [30] and [31] (also refer to [32], [33]). Further details regarding their application to our specific problem can be found in Appendix A.

Alternatively, the space wave component in regions 0 and 2 can be determined by using the stationary phase asymptotic integration technique [34]. In spherical coordinates $O(r, \theta, \varphi)$,

$$\begin{aligned} \bar{E}(\bar{r}) &= \big[\hat{\theta}F_\theta(\theta,\varphi) + \hat{\varphi}F_\varphi(\theta,\varphi)\big]\frac{e^{-ik_0 r}}{r}, \\ \bar{H}(\bar{r}) &= \frac{\nabla \times \bar{E}(\bar{r})}{Z_0} = \frac{1}{Z_0}\big[-\hat{\theta}E_\varphi(\bar{r}) + \hat{\varphi}E_\theta(\bar{r})\big], \end{aligned} \tag{49}$$

where $Z_0 = \sqrt{\mu_0/\varepsilon_0}$. Both $F_\theta(\theta, \varphi)$ and $F_\varphi(\theta, \varphi)$ have closed-form expressions, which are summarized below.

- In region 0:

$$\begin{aligned} F_\theta(\theta,\varphi) &= F^s_\theta(\theta,\varphi) - \frac{ik_0}{4\pi}(Z_0\bar{p}\cdot\hat{\theta} + \bar{m}\cdot\hat{\varphi})e^{ik_0\hat{r}\cdot\bar{r}'}, \\ F_\varphi(\theta,\varphi) &= F^s_\varphi(\theta,\varphi) - \frac{ik_0}{4\pi}(Z_0\bar{p}\cdot\hat{\varphi} - \bar{m}\cdot\hat{\theta})e^{ik_0\hat{r}\cdot\bar{r}'}, \end{aligned} \tag{50}$$

where

$$\begin{aligned} F^s_\theta(\theta,\varphi) &= \frac{2\pi i}{\sin\theta} w^{(1)}_s(0) = -i\pi k_0^3 a_0(\kappa_x,\kappa_y)\sin 2\theta, \\ F^s_\varphi(\theta,\varphi) &= \frac{-2\pi i}{\tan\theta} w^{(2)}_s(0) = i\pi k_0^3 Z_0 b_0(\kappa_x,\kappa_y)\sin 2\theta. \end{aligned} \tag{51}$$

Here, $w^{(j)}_s(z)$ denotes the jth scalar component of $\bar{w}_s(z)$.

- In region 2:

$$\begin{aligned} F_\theta(\theta,\varphi) &= -i\pi k_0^3 a_2(\kappa_x,\kappa_y)e^{ik_0 z_0\cos\theta}\sin 2\theta, \\ F_\varphi(\theta,\varphi) &= i\pi k_0^3 Z_0 b_2(\kappa_x,\kappa_y)e^{ik_0 z_0\cos\theta}\sin 2\theta. \end{aligned} \tag{52}$$

In (51) and (52), (κ_x, κ_y) is the stationary phase point:

$$(\kappa_x, \kappa_y) = (k_0\sin\theta\cos\varphi, k_0\sin\theta\sin\varphi). \tag{53}$$

B. DIPOLES ON TOP OF A GROUNDED SLAB

Refer to the configuration of Fig. 2(b). Now, region 2 is perfectly electrically conducting, and as a result, both E_x and E_y vanish at $z = z_0$. Setting

$$a_2 = k_x\tilde{H}_x(z_0^+) + k_y\tilde{H}_y(z_0^+),$$
$$b_2 = k_y\tilde{H}_x(z_0^+) - k_x\tilde{H}_y(z_0^+), \tag{54}$$

the continuity of $\bar{w}(z)$ at $z = z_1$ leads to the following equation analogous to (48):

$$W_3(z_1, z_0)\Delta \begin{bmatrix} a_2 \\ b_2 \end{bmatrix} - C(-\gamma) \begin{bmatrix} a_0 \\ b_0 \end{bmatrix} = \bar{w}_d(z_1), \tag{55}$$

with

$$\Delta = \begin{bmatrix} 0 & 0 & 1 & 0 \\ 0 & 0 & 0 & 1 \end{bmatrix}^{\intercal}. \tag{56}$$

The expression of the far field in region 0 remains unchanged.

C. HORIZONTAL DIPOLES EMBEDDED IN A SLAB

Here, we consider electric and magnetic dipoles

$$\bar{p} = \hat{x}p_x + \hat{y}p_y, \quad \bar{m} = \hat{x}m_x + \hat{y}m_y$$

positioned at $\bar{r}'(x', y', z')$ inside the bilateral slab of Fig. 2(a) ($z_0 < z' < z_1$, submerged horizontal dipoles).

Region 0 is now source-free, and its field $(\bar{E}_0, \bar{H}_0)$ can be expressed in terms of two scalar potentials, π_{e0} and π_{m0}, with Fourier transforms:

$$\tilde{\pi}_{e0}(z) = a_0 e^{-\gamma(z-z_1)}, \quad \tilde{\pi}_{m0}(z) = b_0 e^{-\gamma(z-z_1)}. \tag{57}$$

Here a_0 and b_0 are coefficients to be determined. The corresponding vector variable $\bar{w}_0(z)$—defined as in (26) but with the index 1 replaced by 0 in both (25) and (26)—is given by

$$\bar{w}_0(z) = C(-\gamma) \begin{bmatrix} a_0 \\ b_0 \end{bmatrix} e^{-\gamma(z-z_1)}. \tag{58}$$

For the vector variable $\bar{w}_1(z)$ associated with the field in region 1 ($z_0 \le z \le z_1$), we can write

$$\bar{w}_1(z) = \begin{cases} W_3(z, z_0)\bar{w}_1(z_0), & z_0 \le z < z' \\ W_3(z, z_1)\bar{w}_1(z_1), & z' < z \le z_1. \end{cases} \tag{59}$$

The field representation in region 2 remains unchanged.

By applying the boundary conditions at $z = z_0$, $z = z_1$, and $z = z'$, we obtain the linear algebraic system:

$$W_3(z', z_0)C(\gamma) \begin{bmatrix} a_2 \\ b_2 \end{bmatrix} - W_3(z', z_1)C(-\gamma) \begin{bmatrix} a_0 \\ b_0 \end{bmatrix} = \bar{w}_d, \tag{60}$$

where

$$\bar{w}_d = -\frac{1}{4\pi^2} e^{ik_x x' + ik_y y'} \begin{bmatrix} -k_x m_y + k_y m_x \\ -k_y m_y - k_x m_x \\ k_x p_y - k_y p_x \\ k_y p_y + k_x p_x \end{bmatrix}. \tag{61}$$

For dipoles embedded in the grounded slab of Fig. 2(b), we obtain the following linear algebraic system analogous to (60):

$$W_3(z', z_0)\Delta \begin{bmatrix} a_2 \\ b_2 \end{bmatrix} - W_3(z', z_1)C(-\gamma) \begin{bmatrix} a_0 \\ b_0 \end{bmatrix} = \bar{w}_d. \tag{62}$$

The expression of the far field in region 2 (case of bilateral slab) remains unchanged. For region 0, we use (49) with $F_\theta(\theta, \varphi)$ and $F_\varphi(\theta, \varphi)$ equated to $F_\theta^s(\theta, \varphi)$ and $F_\varphi^s(\theta, \varphi)$ as defined in (51).

D. DNG SLABS

Our analysis extends to arbitrary isotropic inhomogeneous layers. Initially, we focus on the structure shown in Fig. 2(a) (dipoles over a bilateral slab). We define $\bar{h}^{\text{DPS}} = [a_0, b_0, a_2, b_2]^{\intercal}$ as the column vector containing the unknown coefficients encountered in (48) for a DPS slab with $\varepsilon_1(z) > 0$ and $\mu_1(z) > 0$. We designate the associated transition matrix as $W_3^{\text{DPS}}(z_1, z_0)$. In the case of the DNG counterpart with $-\varepsilon_1(z)$ and $-\mu_1(z)$, we use $\bar{h}^{\text{DNG}}$ and $\bar{W}_3^{\text{DNG}}$. By substituting (42) into (48), we obtain:

$$\Lambda^{\text{DPS}} \cdot \bar{h}^{\text{DPS}} = g(k_x, k_y, z_1)\bar{c}_d, \tag{63}$$

$$(\Lambda^{\text{DNG}} \cdot \bar{h}^{\text{DNG}})^* = \big(g(k_x, k_y, z_1)\bar{c}_d\big)^*, \tag{64}$$

where, for $q \equiv$ DPS and for $q \equiv$ DNG, Λ^q is the 4×4 block matrix

$$\Lambda^q = \begin{bmatrix} -C(-\gamma) & \big| & W_3^q(z_1, z_0)C(\gamma) \end{bmatrix}. \tag{65}$$

The property $A_3^*(z; -\varepsilon_1, -\mu_1) = A_3(z; \varepsilon_1, \mu_1)$ implies:

$$[W_3^{\text{DNG}}(z_1, z_0)]^* = W_3^{\text{DPS}}(z_1, z_0).$$

In the far scattered field, where $(k_x, k_y) = (\kappa_x, \kappa_y)$ [see (53)], $\gamma = ik_0 \cos\theta$, leading to $[C(\pm\gamma)]^* = C(\pm\gamma)$ and $\bar{c}_d^* = \bar{c}_d$. Consequently, $(\Lambda^{\text{DNG}})^* = \Lambda^{\text{DPS}}$, and (64) can be restated as:

$$\Lambda^{\text{DPS}} \cdot (\bar{h}^{\text{DNG}})^* = [g(\kappa_x, \kappa_y, z_1)]^*\bar{c}_d. \tag{66}$$

From (63) and (66), using (43), we deduce:

$$(\bar{h}^{\text{DNG}})^* = e^{-2i[\kappa_x x' + \kappa_y y' - k_0(z'-z_1)\cos\theta]}\bar{h}^{\text{DPS}}. \tag{67}$$

As a result, the relationship between the radiation patterns $\bar{F}^{\text{DNG}}(\theta, \varphi)$ and $\bar{F}^{\text{DPS}}(\theta, \varphi)$ of the far scattered field, whose components are given by (51) and (52), is:

$$[\bar{F}^{\text{DNG}}(\theta, \varphi)]^* = -e^{2i[\kappa_x x' + \kappa_y y' - k_0(z'-z_1)\cos\theta]}\bar{F}^{\text{DPS}}(\theta, \varphi). \tag{68}$$

For the structure in Fig. 2(b) (dipoles over a grounded slab), we substitute $C(\gamma)$ in (65) with Δ and use the definitions in (54) for a_2 and b_2. The final results–equations (67) and (68)–remain unchanged. When a dipole is placed within any of the slabs in Fig. 2, all the previously discussed results and equations remain unchanged. However, in (67) and (68), the phase term $-k_0(z' - z_1)\cos\theta$ should be omitted.

Under the specified conditions, transitioning from a DPS slab to its corresponding DNG slab does not alter the magnitude of the radiation pattern of the far scattered field.

This article has been accepted for publication in IEEE Open Journal of Antennas and Propagation. This is the author's version which has not been fully edited and content may change prior to final publication. Citation information: DOI 10.1109/OJAP.2023.3347704

V. NUMERICAL SCHEME FOR COMPUTING THE TRANSITION MATRICES

In this section, we present an overview of the numerical scheme used to compute the transition matrices W_1, W_2, and W_3 needed in equations (8), (12), (21), (23), (30), (48), (55), (60), and (62). Instead of focusing on a specific case, we provide a unified approach for solving the IVP

$$\frac{dW(z,z_0)}{dz} = A(z)W(z,z_0), \tag{69a}$$

$$W(z_0,z_0) = I, \tag{69b}$$

where I represents the identity matrix of the same order as A. In (69a), A can be A_1, A_2, or A_3, and correspondingly, W represents W_1, W_2, or W_3.

To solve the IVP in (69), we transform it into a second-kind Volterra integral equation (VIE):

$$W(z,z_0) = I + \int_{z_0}^{z} A(z')W(z',z_0)dz' \tag{70}$$

by integrating (69a) from z_0 to z and using (69b). To simplify notation, we introduce a change of variable:

$$z = \alpha + \beta t \quad (-1 < t < 1), \qquad \begin{Bmatrix}\alpha\\ \beta\end{Bmatrix} = \frac{z_1 \pm z_0}{2}. \tag{71}$$

We then define:

$$F(t) = W(z(t),z_0), \quad \Phi(\tau) = A[z(\tau)]. \tag{72}$$

With these definitions, we express (70) as:

$$F(t) = I + \beta \int_{-1}^{t} \Phi(\tau)F(\tau)d\tau. \tag{73}$$

To discretize the VIE (73), we employ the Legendre-Gauss-Radau (LGR) quadrature with nodes at the zeros $t_1 < t_2 < \ldots < t_N = 1$ of $P_{N-1}(t) - P_N(t)$, where $P_k(t)$ is the k-th degree Legendre polynomial. The corresponding weights are:

$$w_j = \frac{1}{N^2}\frac{1+t_j}{[P_{N-1}(t_j)]^2}, \quad j = 1,\ldots,N.$$

Using the expansion:

$$\Phi(\tau)F(\tau) \approx \sum_{k=0}^{N-1} M_k P_k(\tau) \tag{74}$$

with coefficients [27]:

$$M_k = h_k^{-1}\sum_{j=1}^{N} w_j \Phi(t_j)F(t_j)P_k(t_j), \quad h_k = \frac{2}{2k+1}, \tag{75}$$

we derive the discrete counterpart of (73) as:

$$F(t) - \beta\sum_{j=1}^{N}\Phi(t_j)F(t_j)\sum_{k=0}^{N-1}\frac{w_j}{h_k}P_k(t_j)C_k(t) = I. \tag{76}$$

Here [27],

$$C_k(t) = \int_{-1}^{t} P_k(\tau)d\tau = \begin{cases} 1+t, & k=0 \\ \frac{P_{k+1}(t)-P_{k-1}(t)}{2k+1}, & k \geq 1. \end{cases} \tag{77}$$

Subsequently, applying (76) at $t = t_1, t_2, \ldots, t_N$ yields a system of linear algebraic equations:

$$F(t_i) - \beta\sum_{j=1}^{N} w_j b_{ij}\Phi(t_j)F(t_j) = I, \ i = 1,\ldots,N, \tag{78}$$

where

$$b_{ij} = \sum_{k=0}^{N-1} h_k^{-1}P_k(t_j)C_k(t_i). \tag{79}$$

Once we find $\{F(t_i)\}_{i=1}^{N}$ from (78), we can evaluate $F(t)$ at any t in $(-1,1)$ either using (76) or by interpolation [27]:

$$F(t) \approx F^N(t) = \sum_{k=0}^{N-1}\frac{1}{h_k}P_k(t)\sum_{j=1}^{N} w_j P_k(t_j)F(t_j). \tag{80}$$

The property $W(z_1,z_0) = F(1) = F(t_N)$ allows for the direct evaluation of $W(z_1,z_0)$ from (78) without the need for interpolation, justifying our preference for the LGR quadrature method in this paper. This property is also shared by other alternatives, including Gauss-Legendre-Lobatto and Clenshaw-Curtis rules.

A. ERROR ESTIMATE

Let $F(t)$ be the exact solution of (73) and $F^N(t)$ its approximation obtained from either (76) or (80). A convergence analysis (see [35], [36]) provides the following error estimate: If $F \in C^m(-1,1)$, then, for a sufficiently large N, $\|F - F^{N+1}\| = \mathcal{O}(N^{\frac{1}{2}-m})$. When F is analytic ($F \in C^\infty(-1,1)$), $\|F - F^{N+1}\| = \mathcal{O}(e^{cN})$ (c is a constant independent of N), indicating exponential convergence. These properties demonstrate that the proposed technique exhibits the typical convergence behaviour of a spectral method.

The algorithm's spectral convergence rate depends on, and benefits from, the smoothness of the underlying functions, distinguishing it from general-purpose methods that have fixed algebraic convergence rates ($\mathcal{O}(h^p)$); in such methods, p remains constant regardless of the regularity of the function.

Discontinuous (non-smooth) profiles can be addressed in the way outlined in Section VI.

B. SINGULAR PROFILES

For later reference in Section VII.D, we will discuss simple-zero and double-zero inhomogeneity profiles, resulting in corresponding simple-pole and double-pole system matrices

$$A(z) = \frac{1}{(z-z_p)^m}\tilde{A}(z), \quad m = 1 \text{ or } m = 2. \tag{81}$$

Here, z_p represents the pole, and m is its multiplicity. The function $\tilde{A}(z) = (z-z_p)^m A(z)$ is smooth with respect to z. With $z = z(t)$ as in (71), we define:

$$F(t) = W(z(t),z_0), \quad \tilde{\Phi}(\tau) = \tilde{A}[z(\tau)].$$

For $\tilde{\Phi}(\tau)F(\tau)$, we use an expansion of the form (74). Following a procedure similar to the one that led from (69)

to (78), we derive a system of linear algebraic equations analogous to (78):

$$F(t_i) - \beta^{1-m} \sum_{j=1}^{N} w_j b_{ij}^{(m)} \tilde{\Phi}(t_j) F(t_j) = I \tag{82}$$

for $i = 1, \ldots, N$, where

$$b_{ij}^{(m)} = \sum_{k=0}^{N-1} h_k^{-1} P_k(t_j) C_k^{(m)}(t_i) \tag{83}$$

with

$$C_k^{(m)}(t) = \int_{-1}^{t} \frac{P_k(\tau)}{(\tau - t_p)^m} d\tau, \quad t_p = \frac{z_p - \alpha}{\beta} \tag{84}$$

$(-1 < t_p < 1)$. When t_p is in the interval $(-1, t)$, the integral in (84) should be interpreted as the Cauchy principal value for $m = 1$ and in the Hadamard finite-part sense for $m = 2$.

Once we find $\{F(t_i)\}_{i=1}^{N}$ from (82), we can evaluate $F(t)$ at any point, for instance, via interpolation based on (80).

1) Evaluation of $C_k^{(m)}(t)$

We can evaluate $C_k^{(m)}(t)$ using the recurrence relation:

$$P_{k+1}(\tau) = \frac{1}{k+1}[(2k+1)\tau P_k(\tau) - k P_{k-1}(\tau)].$$

This leads to the following expression:

$$\begin{aligned} C_{k+1}^{(m)}(t) =& \frac{2k+1}{k+1}[C_k^{(m-1)}(t) + t_p C_k^{(m)}(t)] \\ & - \frac{k}{k+1} C_{k-1}^{(m)}(t), \quad m = 1, 2. \end{aligned} \tag{85}$$

The term $C_k^{(0)}(t)$ that arises in (85) for $m = 1$ is given by:

$$C_k^{(0)}(t) = \int_{-1}^{t} P_k(\tau) d\tau \equiv C_k(t) \tag{86}$$

with $C_k(t)$ defined in (77). The initial values are:

$$\begin{aligned} C_0^{(1)}(t) &= C_0^{(1)}(t; t_p) = \ln \frac{|t - t_p|}{1 + t_p}, \\ C_1^{(1)}(t) &= C_1^{(1)}(t; t_p) = 1 + t + t_p C_0^{(1)}(t) \end{aligned} \tag{87}$$

and

$$\begin{aligned} C_0^{(2)}(t) &= \int_{-1}^{t} \frac{d\tau}{(\tau - t_p)^2} = \frac{\partial C_0^{(1)}(t; t_p)}{\partial t_p}, \\ C_1^{(2)}(t) &= \int_{-1}^{t} \frac{\tau d\tau}{(\tau - t_p)^2} = C_0^{(1)}(t) + t_p C_0^{(2)}(t). \end{aligned} \tag{88}$$

VI. LAYERED AND ELECTRICALLY THICK SLABS

Our analysis extends to multilayer slabs, such as the one shown in Fig. 3, with the region (z_0, z_1) comprising L inhomogeneous sublayers. The core results—equations (10), (23), (48), (55), (60), and (62)—remain unchanged. Now, when $W = W_i$ with $i = 1, 2, 3$, we compute $W(z_1, z_0)$ by cascading the transition matrices of all the layers:

$$W(z_1, z_0) = W(z_1, \zeta_{L-1}) \ldots W(\zeta_1, z_0). \tag{89}$$

The matrices $W_3(z', z_0)$ and $W_3(z', z_1)$ appearing in (60) and (62) are computed similarly.

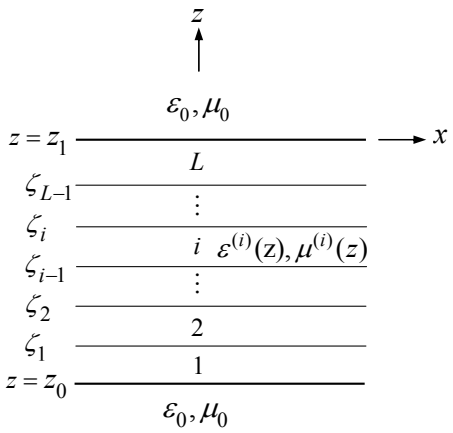

FIGURE 3. Multilayer inhomogeneous slab with L inhomogeneous sublayers.

The convergence of the algorithm relies on the smoothness of $\{\varepsilon^{(i)}(z), \mu^{(i)}(z)\}_{i=1}^{L}$. Exponential convergence is achieved when these functions are analytic.

A. HANDLING DISCONTINUOUS PROFILES

The latter observation offers a simple and efficient method for handling single-layer slabs with discontinuous inhomogeneous profiles: Modelling the slab as a stack of layers by introducing artificial interfaces at the locations of the discontinuities and then applying (89). The algorithm achieves spectral convergence, with the rate depending on the smoothness of the parameters within each sublayer.

B. THICK SLABS

While the model in Fig. 3 primarily focuses on multilayer slabs, it also offers advantages when applied to single, electrically thick slabs. In the case of a single slab, the required quadrature order N increases with the electric size of the slab. As $k_0 d$ becomes larger, the size of the Nyström matrix (N^2) and, consequently, the computational demands can become quite high and potentially prohibitive. To address this challenge, a thick slab can be artificially divided into a stack of L moderate-thickness layers, and the equation (89) can be used. This approach optimally maintains N at a manageable level, significantly enhancing the stability and computational efficiency of the algorithm. For more details, refer to Section VII.

VII. NUMERICAL RESULTS AND COMPARISONS

In this section, we present numerical examples to validate the algorithms and demonstrate the high accuracy and flexibility of the proposed method. For scattering problems involving E (H) polarized plane-waves, we assume that $(\varepsilon_2, \mu_2) = (\varepsilon_0, \mu_0)$, and use an incident field amplitude of $E_0 = 1V/m$ ($H_0 = 1A/m$), unless stated otherwise.

The computer programs were implemented in Mathematica 10.4, which employs machine precision arithmetic as the default setting. It uses double-precision floating-point

numbers with approximately 16 decimal digits of precision. However, Mathematica also supports variable precision arithmetic, allowing users to specify their desired precision for numerical calculations. Precision can be set either globally, using the global variable `$PreRead`, or on a per-expression basis using the `SetPrecision` function. In our work, we consistently used a precision setting of 17 digits for all examples, except for Table 1 and Fig. 8.

A. CONVERGENCE ANALYSIS

In Fig. 4, we demonstrate the convergence of the algorithm by plotting the base-10 logarithm of the relative errors of $|R|$ and $|T|$ against the quadrature order N. These results pertain to the E-case with $k_0 d = \pi$ and $\psi = \pi/4$. We consider six distinct inhomogeneity profiles, labelled as Case I through Case VI, each of which has exact analytical solutions available (see Appendix B). The relative error ϵ for $X = |R|$ and $X = |T|$ is defined as $\epsilon = |(X - X^{exact})/X^{exact}|$. The figure illustrates exponential convergence, consistently achieving an error on the order of 10^{-16}, comparable to the round-off error, with the appropriate selection of N.

For a deeper insight into the convergence behavior of the method, Table 1 presents the relative error of $|R|$ for various quadrature orders N with parameter values matching those in Fig. 4. These computations use high-precision arithmetic. Notably, Table 1 reveals a phenomenon of super-convergence: doubling the value of N yields more than double the number of correct digits in the computed reflection coefficient. This observation, combined with the results from Fig. 4, suggests that the algorithm's accuracy is only limited by the employed machine precision. These findings emphasize the exceptional precision and reliability of the method.

TABLE 1. Convergence of relative error for $|R|$ in the E-case with $k_0 d = \pi$ and $\psi = \pi/4$. Constitutive parameters $\varepsilon_{r1}(z)$ and $\mu_{r1}(z)$ in Case I–Case III are the same as in Fig. 4.

	Relative Error		
N	Case I	Case II	Case III
8	0.305575	0.00996931	0.00349806
16	1.6634×10^{-7}	3.85954×10^{-10}	2.95448×10^{-10}
32	2.35123×10^{-32}	4.53615×10^{-31}	9.15876×10^{-29}
64	2.07652×10^{-102}	1.03709×10^{-83}	2.26694×10^{-73}
128	1.41282×10^{-281}	8.8053×10^{-210}	3.39653×10^{-174}

In Fig. 4, the slab had a thickness falling within the resonance region. However, the results shown in Fig. 5, with $k_0 d$ at $20\pi, 200\pi, 500\pi$, emphasize that the algorithm can handle significantly thicker slabs. By employing the model shown in Fig. 3 and appropriately selecting the number of artificial layers L and the quadrature order N, we consistently achieve an error on the order of 10^{-16} in all cases, underlying the reliability of the method for very thick slabs.

In all previous examples, the profiles were continuous spatial functions. To explore the algorithm's behavior in the presence of discontinuous parameters, we now consider a slab with $\mu_{r1} = 1$ and a relative permittivity given by:

$$\varepsilon_{r1}(z) = \begin{cases} 2 + 2(z+d)^2/d^2, & -d \le z \le -\frac{d}{2} \\ \frac{5}{4}d^2/(z+d)^2, & -\frac{d}{2} < z < 0. \end{cases}$$

This profile has a second-kind (jump) discontinuity at $z = -d/2$. Following the framework outlined in Section VI, we use the model of Fig. 3 with $L = 2$, introducing an artificial interface at $z = \zeta_1 = -d/2$, and use (89). In Fig. 6, we present the relative errors of $|R|$ and $|T|$ as N increases for the E-case, with $k_0 d = 5\pi$ and $\psi = \pi/4$, demonstrating exponential convergence similar to our previous examples.

In Fig. 7, we show the base-10 logarithm of the relative error for $|\bar{F}(\theta, \varphi)|$, representing the radiation pattern of an electric dipole in the configuration of Fig. 2(a). We used the model from Fig. 3 with 10 artificial layers (L=10). The parameters values are: $(\theta, \varphi) = (\pi/3, \pi/4)$, $\bar{p} = (\hat{x} + \sqrt{3}\hat{y})/2$, $k_0 d = 2\pi$, and $\bar{r}' = (0, 0, 0)$. The relative permittivity and permeability profiles, shown in the inset, are $\varepsilon_{r1} = \exp(-k_0 z)$ and $\mu_{r1} = \exp[k_0(d + z)]$. The convergence remains exponential, with the relative error reaching approximately 10^{-15} when an appropriate value of N is chosen.

In Fig. 8, we compare the convergence of our algorithm with that of the widely used SA method (staircase approximation) for the E-case with parameters $\psi = \pi/4$, $k_0 d = 20\pi$, $\varepsilon_{r1} = 3 + \cos[k_0(z + d)]$, and $\mu_{r1} = 1$. In Fig. 8(a), the relative error is plotted against $N^2 L$ for our algorithm and against L for the SA method. Notably, SA requires nearly $L = 10^6$ layers to achieve a relative error of 10^{-13}, whereas our algorithm, with $L = 20$ and $N = 70$, attains an error of 10^{-100}. Moving to Fig. 8(b), we compare the time required for both methods to reach a set accuracy level, further highlighting the superiority of our approach.

B. APPLICATION EXAMPLE: PHOTONIC CRYSTAL

As mentioned in the Introduction, inhomogeneous slabs with periodically modulated refractive indices can function as 1D EM band-gap structures. In Fig. 9, we explore this possibility with $d = 1\text{m}$, $\varepsilon_{r1} = 2 + 15\sin^4(30\pi z)$ and $\mu_{r1} = 2$. In Fig. 9(a), we show the first three band gaps in the transmittance $|T|^2$ for $\psi = 0$, indicating equal transmittance for both E and H polarizations. Focusing on the lower portion of the first band gap, in Figs. 9(b) and 9(c), we depict transmittance variations with the angle of incidence in the E and H case, respectively. Notably, within the range $22 < k_0 d < 32$, transmittance remains consistently below 10^{-8} for both polarizations, regardless of the angle of incidence.

C. SCATTERING ON A PLASMA SLAB

We now consider an inhomogeneous cold collisional plasma layer with relative permittivity

$$\varepsilon_{r1}(z) = 1 - \frac{\frac{\omega_p^2(z)}{\omega^2}}{1 - i\frac{\nu_{en}(z)}{\omega}}. \tag{90}$$

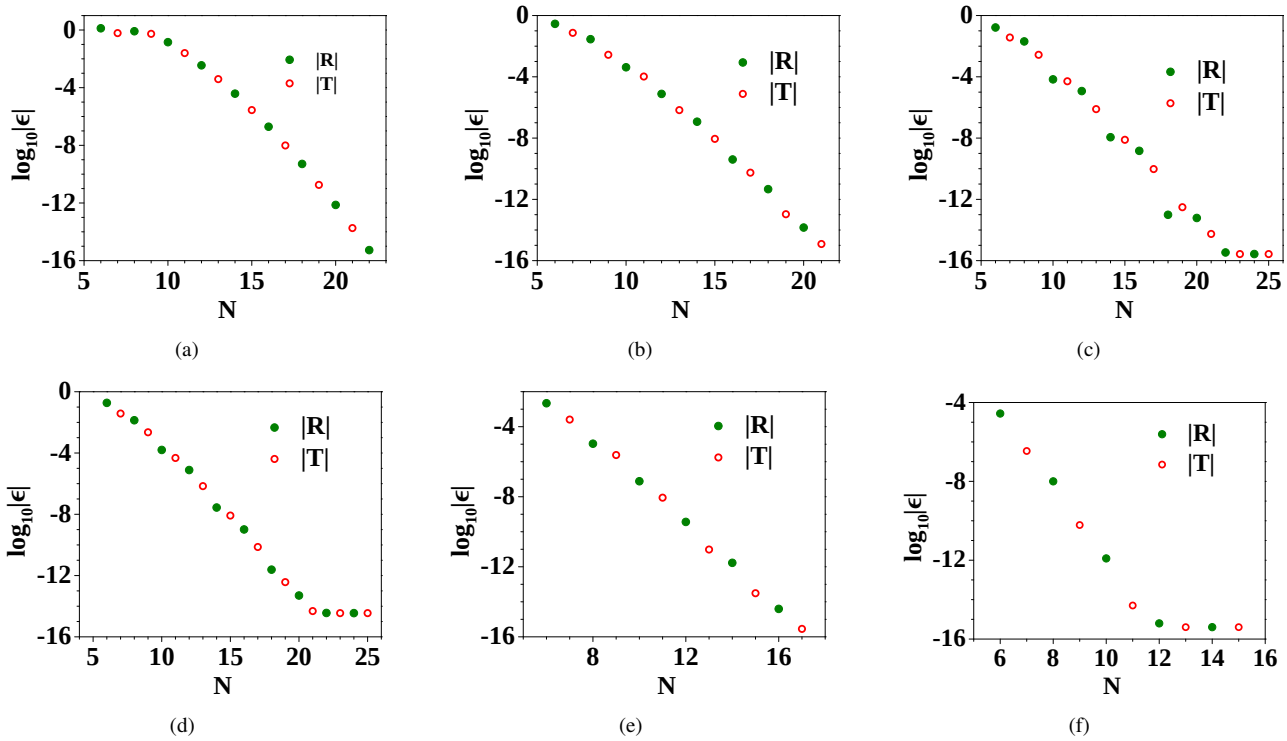

FIGURE 4. $\log_{10}$ **of relative error for** $|R|$ **and** $|T|$ **versus quadrature order** N **in the E-case with** $k_0 d = \pi$ **and** $\psi = \pi/4$**. (a) Case I:** $\varepsilon_{r1}(z) = e^{-k_0 z}$, $\mu_{r1}(z) = e^{k_0(z+d)}$**. (b) Case II:** $\varepsilon_{r1}(z) = 1 + 2[k_0(z+d)]^2$, $\mu_{r1} = 1$**. (c) Case III:** $\varepsilon_{r1}(z) = 1 + e^{k_0(z+d)}$, $\mu_{r1} = 1$**. (d) Case IV:** $\varepsilon_{r1} = 1$, $\mu_{r1}(z) = e^{k_0(z+d)}$**. (e) Case V:** $\varepsilon_{r1}(z) = 3 + \cos[k_0(z+d)]$, $\mu_{r1} = 1$**. (f) Case VI:** $\varepsilon_{r1}(z) = 2d/(z+2d)$, $\mu_{r1}(z) = (z+2d)/d$.

Here, ν_{en} is the frequency of electron-neutral collisions, and ω_p is the angular plasma frequency: $\omega_p = \sqrt{e^2 n_e(z)/\varepsilon_0 m}$, where n_e, e, and m stand for the plasma density, electron charge, and electron mass, respectively. For generality, we assume that both n_e and ν_{en} vary spatially with distributions:

$$n_e(z) = n_0\Big[1 - \big(1 + \frac{2z}{d}\big)^2\Big]^2,$$
$$\nu_{en}(z) = \nu_0 e^{-\alpha(1+2\frac{z}{d})^2} \tag{91}$$

shown in Fig. 10. Here, n_0 is a constant, and the parameter α can be set to either $\alpha = 0$ (in which case $\nu_{en}(z) = \nu_0$ remains constant) or $\alpha = 1$.

In Fig. 11, we validate the algorithm for $\alpha = 0$, resulting in a constant $\nu_{en}(z)$ set equal to ν_0. The figure displays reflectance ($|R|^2$), transmittance ($|T|^2$), and absorbance ($A = 1 - |R|^2 - |T|^2$) as functions of ν_{en}/f with $\psi = 0$, $f = 2.85$ GHz, $n_0 = 1.00755 \times 10^{17}$ m^{-3}, and $d = 10$ cm. Our results perfectly match those in Fig. 3 of Ref. [18].

In Fig. 12, we analyze reflectance, transmittance, and absorbance as functions of frequency for two ν_0 values (1 GHz and 10 GHz) under both $\alpha = 0$ and $\alpha = 1$. We maintain $n_0 = 10^{18}$ m^{-3} and $d = 10$ cm constant. Notably, the curves associated with $\nu_{en} = \nu_0 = 1$ GHz (corresponding to $\alpha = 0$) closely resemble those in Fig. 4 of Ref. [18]. The ability to control the scattering characteristics by varying ν_0 is evident.

Fig. 13 shows the dependence of reflectance and absorbance on frequency (f) and slab thickness (d) in the E-case for $\psi = 0$, $\alpha = 1$, and $n_0 = 10^{18}$ m^{-3}. In Figs. 13(a) and 13(c), $\nu_0 = 1$ GHz, while in Figs. 13(b) and 13(d), $\nu_0 = 10$ GHz.

For future reference, Figs. 14 and 15 display the variation of the reflectance, transmittance, and absorbance with frequency (f) and incidence angle (ψ) in the E and H cases, respectively, for $\nu_0 = 1$ GHz, $n_0 = 10^{18}$ m^{-3}, $d = 10$ cm, and $\alpha = 1$.

D. FIELD ENHANCEMENT IN EPSILON-CROSSING-ZERO FILMS

Field enhancement occurs in structures with near-zero parameters [37]. To illustrate, consider a thin ($k_0 d << 1$) homogeneous slab with permittivity $\varepsilon_0\varepsilon_r$, positioned in air and illuminated by an H-polarized wave. The boundary conditions $E_z(z_1^-) = E_z(z_1^+)/\varepsilon_r$ and $E_z(z_0^+) = E_z(z_0^-)/\varepsilon_r$ signify an amplification of $|E_z|$ within the slab, inversely proportional to ε_r. As ε_r approaches zero, this phenomenon intensifies, leading to significant energy confinement.

To investigate the field enhancement effect in inhomogeneous slabs with permittivity profiles that exhibit zero crossings, Fig. 16 presents the distribution of $|E_z(z)|$ within a plasma slab surrounded by air in the H-case, with parameters $\psi = \pi/4$, $k_0 d = \pi$, $Z_0 H_0 = 1$, $n_0 = 10^{18}$ m^{-3}. The relative permittivity, defined as:

$$\varepsilon_{r1}(z) = 1 - \omega_p^2(z)/\omega^2, \tag{92}$$

corresponds to (90) with $\nu_0 = 0$ in (91).

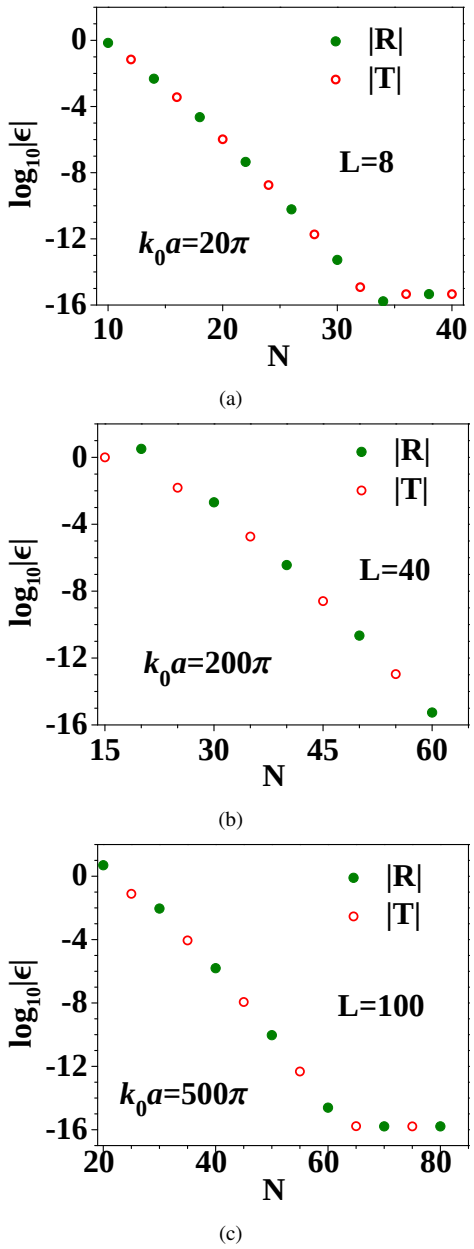

FIGURE 5. $\log_{10}$ **of relative error for** $|R|$ **and** $|T|$ **versus** N **in the E-case with** $\psi = \pi/4$, $\varepsilon_{r1} = 3 + \cos[k_0(z+d)]$ **and** $\mu_{r1} = 1$. **(a)** $k_0 d = 20\pi$, **(b)** $k_0 d = 200\pi$, **(c)** $k_0 d = 500\pi$.

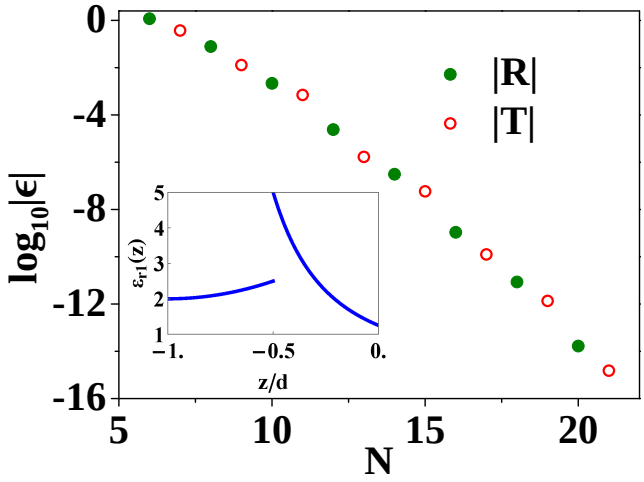

FIGURE 6. $\log_{10}$ **of the relative error for** $|R|$ **and** $|T|$ **versus** N **in the E-case with a discontinuous permittivity profile (inset) at** $k_0 d = 5\pi$ **and** $\psi = \pi/4$.

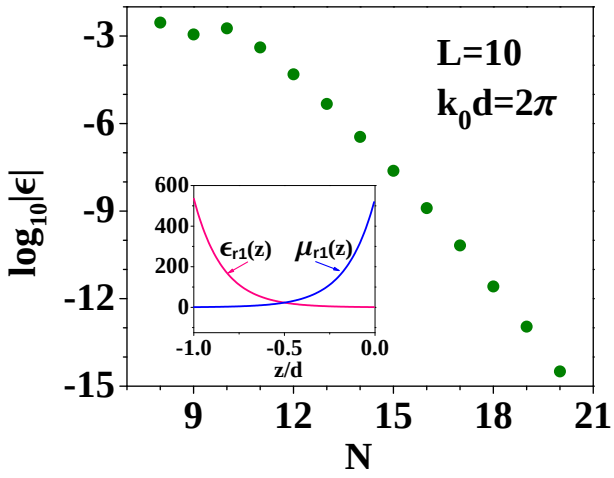

FIGURE 7. $\log_{10}$ **of relative error for** $|\bar{F}(\theta,\varphi)|$ **with** $(\theta,\varphi) = (\pi/3, \pi/4)$, $\bar{p} = (\hat{x} + \sqrt{3}\hat{y})/2$, $k_0 d = 2\pi$, $\bar{r}' = (0,0,0)$, $\varepsilon_{r1} = \exp(-k_0 z)$, $\mu_{r1} = \exp[k_0(d+z)]$.

In Fig. 16(a), we select the circular frequency as $\omega = \omega_p(-d/2) = 5.64146 \times 10^{10}$ rad/s. With this choice, $\varepsilon_{r1}(z)$ takes the form $\varepsilon_{r1}(z) = (d+2z)^2\left(d^2 - 4dz - 4z^2\right)/d^4$ (inset), exhibiting a double zero at $z = -d/2$. As a result, substantial field confinement occurs at the slab's mid-plane. The results in Fig. 16(a) were obtained using the algorithm outlined in Section V.B (case $m = 2$).

In Fig. 16(b), we have chosen $\omega = 5.5 \times 10^{10}$ rad/s. For this specific choice, $\varepsilon_{r1}(z)$ has zeros at $z/d = -0.4208244$ and $z/d = -0.5791756$ (see inset), leading to twin field confinement at these two planes. The results in Fig. 16(b) were obtained using the algorithm in Section V.B (case $m = 1$).

E. DIPOLE RADIATION OVER A METAMATERIAL SLAB

For an electric dipole $\bar{p} = 1\hat{y}$ (in Am) positioned at $\bar{r}' = (0, 0, -d/2)$ within the bilateral slab of Fig. 2(a), Fig. 17 illustrates the amplitude of the radiation pattern $|\bar{F}(\theta,\varphi)|$ in both the E-plane ($\varphi = 0$) and the H-plane ($\varphi = \pi/2$). The parameter values are: $k_0 = 1$, $k_0 d = 2\pi$, $\varepsilon_{r1}(z) = \exp(-k_0 z)$, and $\mu_{r1} = \exp[k_0(z+d)]$. Our computed results precisely match the corresponding analytical solutions.

For a dipole radiating on top of a grounded homogeneous DNG slab, in Fig. 18, we show $20\log_{10}|\bar{F}(\theta,\varphi)|$, (a) in the E–plane and (b) in the H–plane with $\bar{p} = 10^{-3}\hat{x}$ (in Am), $f = 5.943$ GHz, $d = 60$ mm, $\bar{r}' = (0,0,0)$, $\varepsilon_{r1} = -1.831$, and $\mu_{r1} = -0.0238$. The agreement with Ref. [38] is excellent.

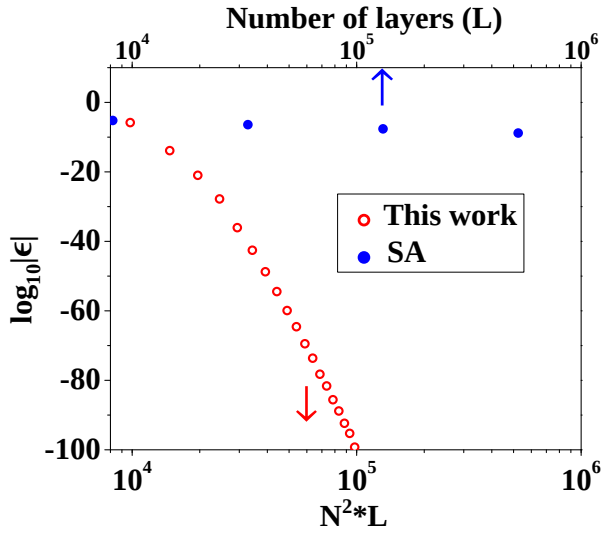

(a)

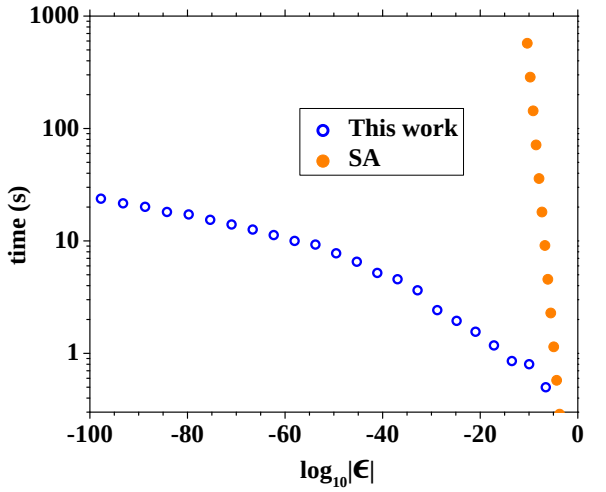

(b)

FIGURE 8. **(a)** $\log_{10}$ **of relative error for** $|R|$ **versus the number of layers L (SA), or** N^2L **(this work). (b) Time required to achieve a preset level of accuracy.** E**-case,** $\psi = \pi/4$**,** $k_0 d = 20\pi$**,** $\varepsilon_{r1} = 3 + \cos[k_0(z+d)]$**,** $\mu_{r1} = 1$**.**

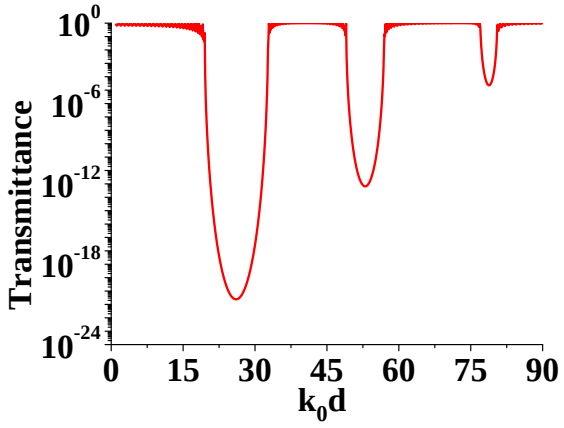

(a)

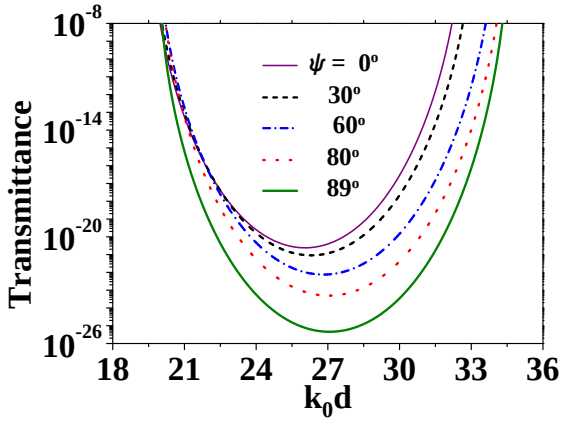

(b)

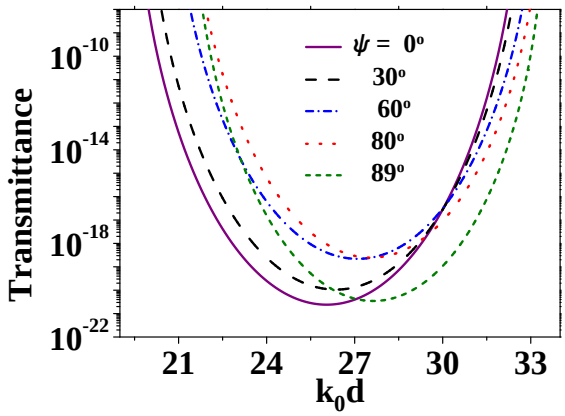

(c)

FIGURE 9. **Transmittance (**$|T|^2$**) vs.** $k_0 d$ **for** $\varepsilon_{r1} = 2 + 15\sin^4(30\pi z)$ **and** $\mu_{r1} = 2$**. (a)** $\psi = 0$ **for both E- and H-polarization. (b) E-case with various** ψ **values:** $0^\circ, 30^\circ, 60^\circ, 80^\circ, 89^\circ$**. (c) H-case with the same** ψ **values.**

For a μ-near-zero grounded metamaterial slab with $\varepsilon_{r1} = 1.2$ and $\mu_{r1} = 0.01$, Fig. 19 illustrates the power pattern $P(\theta) = |\bar{F}(\theta, \varphi)|^2/(2Z_0)$ (in dB) at the principal planes $\varphi = 0$ and $\varphi = \pi/2$. In Fig. 19(a), the pattern is shown for an electric dipole $\bar{p} = 1\hat{y}$ (in Am) located at $\bar{r}' = (0, 0, -d/2)$, while in Fig. 19(b) it is shown for a magnetic dipole $\bar{m} = Z_0\hat{y}$ (in Vm) located at $\bar{r}' = (0, 0, -d)$. The operating frequency is $f = 9.122$ GHz, and the slab thickness is $d = 75$ mm. Our results are indistinguishable from those presented in Ref. [39].

F. SOME FEATURES OF A DIPOLE DRIVEN PLASMA ANTENNA

At the frequency of $f = 8$ GHz, in Fig. 20, we show the radiation patterns $|\bar{F}(\theta, \varphi)|$ (in dB) in the E-plane ($\varphi = 0$) and H-plane ($\varphi = \pi/2$) for horizontal electric [$\bar{p} = 0.001\hat{x}$ in Am, Figs. 20(a) and 20(b)] and magnetic

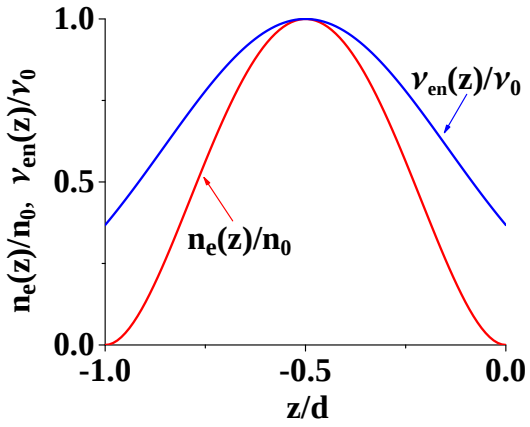

FIGURE 10. **Profiles of inhomogeneity: $n_e(z)$ and $\nu_{en}(z)$.**

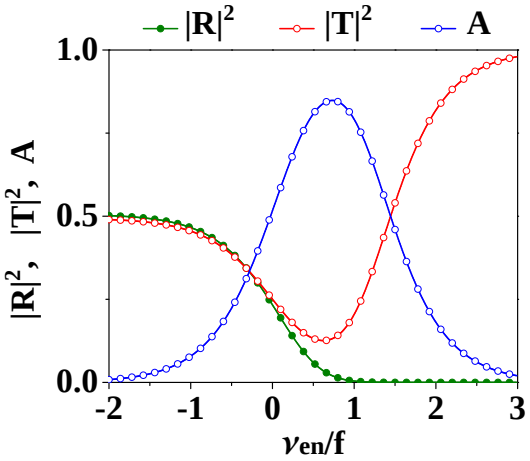

FIGURE 11. **Reflectance, Transmittance, and Absorbance vs. ν_{en}/f at $\psi = 0$, $\alpha = 0$, $f = 2.85$ GHz, $d = 10$ cm, and $n_0 = 1.00755 \times 10^{17}$ m^{-3}. Solid lines: this work, open and solid circles: Ref. [18].**

[$\bar{m} = 1\hat{x}$ in Vm, Figs. 20(c) and 20(d)] dipoles. The dipoles are positioned at the upper interface $z = 0$ of either a bilateral plasma slab (solid lines) or a grounded plasma slab (dotted lines); the other parameter values are: $\bar{r}' = (0, 0, 0)$, $d = 10$ cm, $\alpha = 1$, $\nu_0 = 1$ GHz, and $n_0 = 10^{18}$ m^{-3}. Additionally, Figs. 20(e) and 20(f) display similar radiation patterns $|\bar{F}(\theta, \varphi)|$ on the $\varphi = \varphi_0$ plane, where φ_0 can be any constant value, corresponding to vertical electric and magnetic dipoles. Notably, the radiation patterns for the bilateral slab align perfectly with those of the grounded slab. This alignment is easily explained by examining the plots in Figs. 14(b) and 15(b), which reveal that, at $f = 8$ GHz, the transmittance is extremely small for any angle of incidence. This indicates that the interface $z = z_0 = -d$ behaves like a perfectly conducting plane. Based on the results in Fig. 20, we can conclude that, at the selected operating frequency, the bilateral plasma slab of Fig. 2(a) serves as a practical implementation of the grounded plasma slab of Fig. 2(b), eliminating the need for any conductive elements.

CONCLUSIONS

We have introduced a simple yet highly accurate numerical scheme for studying scattering of plane and spherical electromagnetic waves on inhomogeneous materials, plasma, and metamaterial slabs. While our primary focus has been on scattering and radiation, the algorithms can also address the related propagation problems, as well as complex frequency eigenvalue and eigenvalue lasing problems [40]. Furthermore, these algorithms can be extended to slabs containing complex inhomogeneous media that can be anisotropic, chiral, or bi-anisotropic. Such an extension would enable investigations into intricate EM problems across a broad spectrum of innovative materials and configurations.

APPENDIX A
FAR SCATTERED FIELD

Here, we provide an overview of the application of the method of contour integration to our specific problem. We focus on a vertical electric dipole ($\bar{p} = \hat{z}p$) located at $\bar{r}' = \hat{z}z'$ above the slab in Fig. 2(a), and limit our discussion to the analytical evaluation of the Hertz potential π^s_{e0} as defined in Section IV.A.3. The approach for evaluating the remaining Hertz potentials and the field within the slab is similar.

A closer examination of (78) reveals that the transition matrix W_3 follows the structure noted in [11]:

$$W_3 = \begin{bmatrix} w_{11} & 0 & 0 & w_{14} \\ 0 & w_{22} & w_{23} & 0 \\ 0 & w_{32} & w_{33} & 0 \\ w_{41} & 0 & 0 & w_{44} \end{bmatrix}. \tag{93}$$

The elements w_{ij} are analytic functions of λ^2 (or equivalently, of γ^2). Once we determine a_0 from (48) using (93), we can derive $\tilde{\pi}^s_{e0}$ from (46) as follows:

$$\tilde{\pi}^s_{e0}(\gamma, z) = \frac{ip}{8\pi^2\omega\varepsilon_0}\frac{\mathcal{N}(\gamma)}{\gamma\mathcal{D}(\gamma)}e^{-\gamma(z+z'-2z_1)}, \tag{94}$$

where,

$$\frac{\mathcal{N}(\gamma)}{\mathcal{D}(\gamma)} = (\omega\varepsilon_0)^2 w_{14} \pm \gamma^2 w_{41} - i\omega\varepsilon_0\gamma(w_{11} \mp w_{44}). \tag{95}$$

To evaluate the inverse Fourier transform π^s_{e0} of $\tilde{\pi}^s_{e0}$, we introduce a change of variables:

$$k_x = \lambda\cos\beta, k_y = \lambda\sin\beta, \quad x = \rho\cos\varphi,\ y = \rho\sin\varphi$$

($0 \le \beta, \varphi \le 2\pi$) and follow the procedure outlined in [31]. When $z_1 = 0$, as in Fig. 2, we obtain:

$$\begin{aligned}\pi^s_{e0}(\bar{r}) &= \iint_{-\infty}^{+\infty} e^{-i(k_x x + k_y y)}\tilde{\pi}^s_{e0}(\gamma, z)\, dk_x\, dk_y \\ &= \frac{ip}{8\pi\omega\varepsilon_0}\int_{-\infty}^{\infty} H_0^{(2)}(\lambda\rho)\frac{\mathcal{N}(\gamma)}{\gamma\mathcal{D}(\gamma)}e^{-\gamma(z+z')}\lambda d\lambda.\end{aligned} \tag{96}$$

The original inverse transform path C_0 takes the form shown in Fig. 21, accounting for the presence of the two branch points $\pm k_0$ of the multivalued function $\gamma(\lambda)$ and the surface wave poles of the integrand. These poles correspond

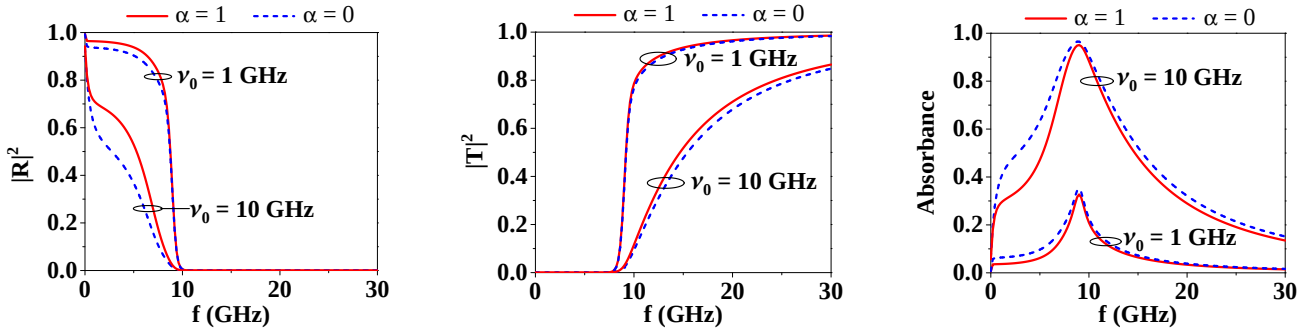

FIGURE 12. **(a) Reflectance, (b) Transmittance, and (c) Absorbance vs. frequency for $\psi = 0$, $n_0 = 10^{18}$ m^{-3}, $d = 10$ cm. Solid lines: $\alpha = 1$, dotted lines: $\alpha = 0$.**

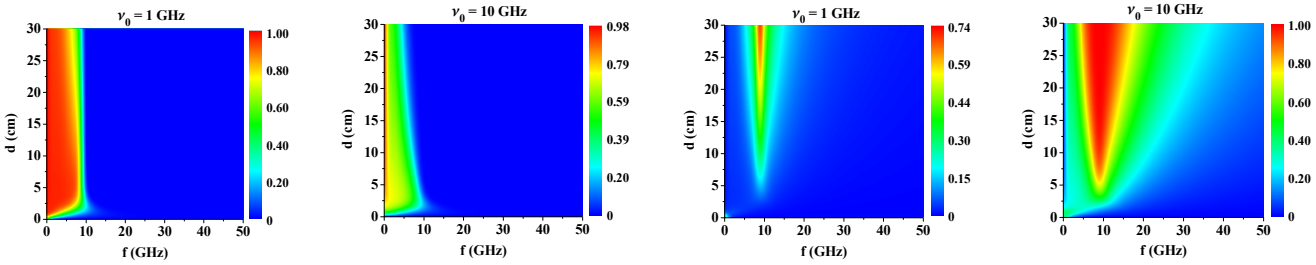

FIGURE 13. **Reflectance (a, b) and Absorbance (c, d) as a function of frequency and slab thickness in the E-case for $\psi = 0$, $\alpha = 1$, and $n_0 = 10^{18}$ m^{-3}. Subfigures (a, c) are for $\nu_0 = 1$ GHz, while subfigures (b, d) are for $\nu_0 = 10$ GHz.**

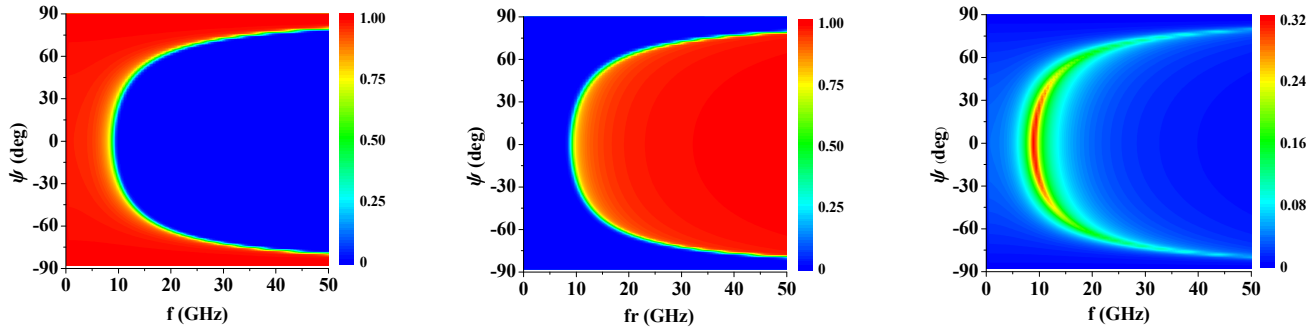

FIGURE 14. **E-polarization: (a) Reflectance, (b) Transmittance, and (c) Absorbance vs. frequency and angle of incidence for $n_0 = 10^{18}$ m^{-3}, $d = 10$ cm, $\alpha = 1$, $\nu_0 = 1$ GHz.**

to the roots $\lambda = \pm\beta_1, \ldots, \pm\beta_n$ of $\mathcal{D}[\gamma(\lambda)] = 0$, representing the dispersion equation for the supported TM^y modes. (*Note*: The pole configuration illustrated in Fig. 21 is specific to the lossless case. When the slab exhibits loss, these poles shift away from the Re(λ) axis.) The branch cuts of γ extend to infinity as illustrated in the figure. Additionally, the Hankel function introduces a branch point at $\lambda = 0$ with the corresponding branch cut extending to infinity along the positive Im(λ) axis.

Next, we deform C_0 as shown in Fig. 21 and apply Cauchy's residue theorem on the formed closed path $C_0 + C_1 + C_2$. Working as in Refs. [30]–[32], we obtain:

$$\pi^s_{e0}(\bar{r}) = -\int_{C_2} f(\lambda)d\lambda - 2\pi i \sum_{j=1}^{n} \operatorname*{Res}_{\lambda\to\beta_j}(f, \beta_j), \qquad (97)$$

$$f(\lambda) = \frac{ip}{8\pi\omega\varepsilon_0} H_0^{(2)}(\lambda\rho)\frac{\lambda\mathcal{N}(\gamma)}{\gamma\mathcal{D}(\gamma)} e^{-\gamma(z+z')},\ \gamma = \gamma(\lambda).$$

A. SPACE-WAVE COMPONENT

The first term in (97) which contains the integral over C_2 represents the space-wave component of the potential. A steepest descent evaluation of this integral, as outlined in

This article has been accepted for publication in IEEE Open Journal of Antennas and Propagation. This is the author's version which has not been fully edited and content may change prior to final publication. Citation information: DOI 10.1109/OJAP.2023.3347704

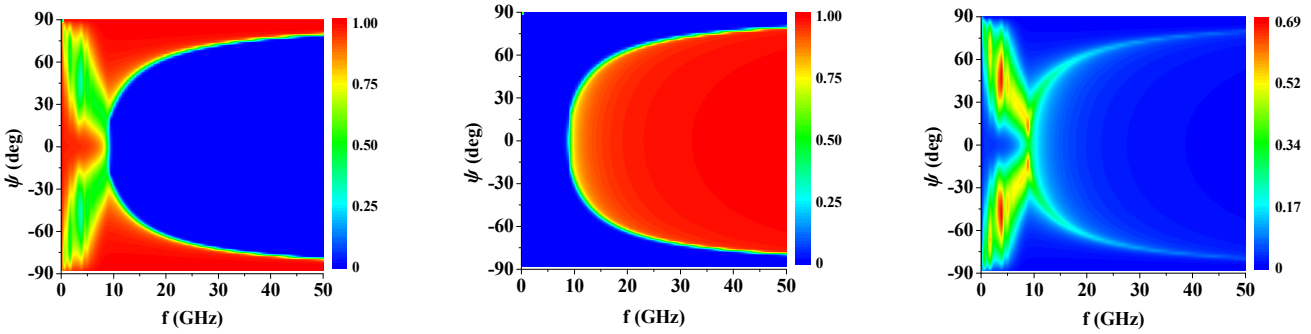

FIGURE 15. **H-polarization: (a) Reflectance, (b) Transmittance, and (c) Absorbance vs. frequency and angle of incidence for $n_0 = 10^{18}$ m^{-3}, $d = 10$ cm, $\alpha = 1$, $\nu_0 = 1$ GHz.**

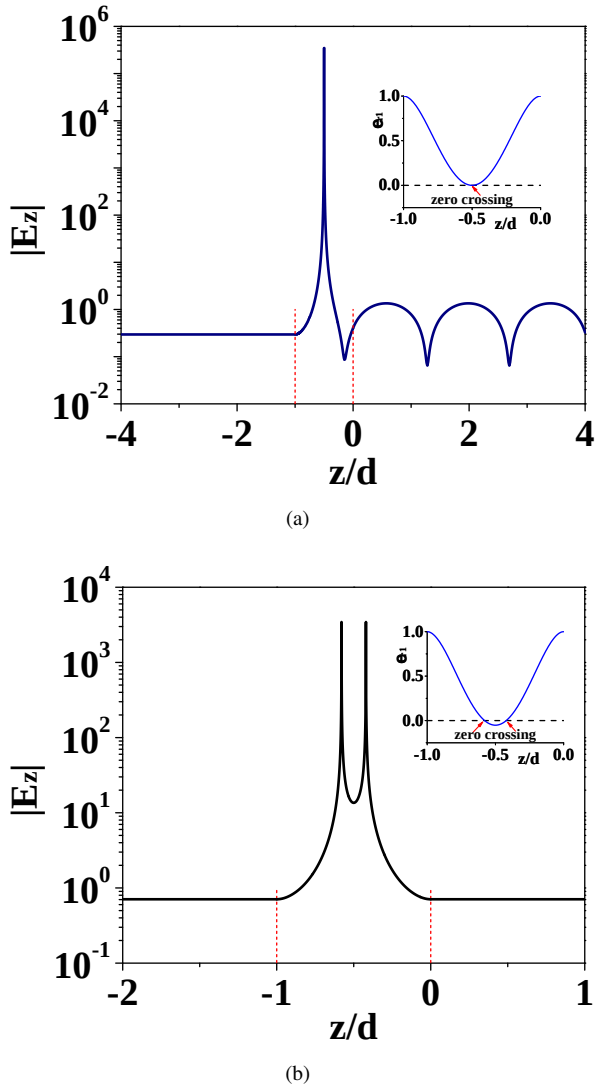

FIGURE 16. **Field distribution $|E_z(z)|$ for an Epsilon crossing zero plasma slab in the H-case for $\psi = \pi/4$, $k_0 d = \pi$, $Z_0 H_0 = 1$, and $n_0 = 10^{18}$ m^{-3}. (a) $\omega = \omega_p(-d/2) = 5.64146 \times 10^{10}$ and (b) $\omega = 5.5 \times 10^{10}$ (in rad/s). The relative permittivity is given in (92).**

Ref. [31] and valid for large distances from the dipole, results in the closed-form expression:

$$\pi^s_{e0}(\bar{r}) = \frac{ip}{4\pi\omega\varepsilon_0}\frac{\mathcal{N}(\gamma)}{\mathcal{D}(\gamma)}\frac{e^{-ik_0 r-\gamma z'}}{r}, \quad \gamma = ik_0\cos\theta. \quad (98)$$

The correctness of (98) has been checked via an independent derivation using the stationary phase integration technique.

B. SURFACE-WAVE COMPONENT

The second term in (97) represents the surface-wave component of the potential. Here, for large distances from the dipole, it is appropriate to use the large-argument asymptotic form: $H_0^{(2)}(\lambda\rho) \sim \sqrt{\frac{2i}{\pi\lambda\rho}}e^{-i\lambda\rho}$. In obtaining the $\underset{\lambda\to\beta_j}{\text{Res}}$, we employ the chain rule:

$$\frac{d\mathcal{D}[\gamma(\lambda)]}{d\lambda} = \frac{d\mathcal{D}(\gamma)}{d\gamma}\frac{d\gamma}{d\lambda} = \frac{\lambda}{\gamma}\mathcal{D}'(\gamma).$$

The resulting expression for the surface-wave component is:

$$\pi^s_{e0}(\bar{r}) = \frac{p}{4\omega\varepsilon_0}\sqrt{\frac{2i}{\pi\rho}}\sum_{j=1}^{n}\frac{\mathcal{N}(\gamma_j)}{\sqrt{\beta_j}\,\mathcal{D}'(\gamma_j)}e^{-i\beta_j\rho-\gamma_j(z+z')} \quad (99)$$

with $\gamma_j = \{\beta_j^2 - k_0^2\}^{1/2}$. The term $\mathcal{D}'(\gamma_j)$ can be easily obtained from (95) provided the derivative $w'_{ij}(\gamma)$ can be computed.

1) Computation of $\{\beta_j\}_{j=1}^n$

As previously mentioned, the elements w_{ij} with $1 \le i, j \le 4$ of the transition matrix W_3 are analytic functions of λ^2 (or γ^2). Consequently, $\mathcal{D}(\gamma)$, as defined in (95), is an analytic (i.e., pole free) function of γ. This property enables us to compute the roots $\{\gamma_j\}_{j=1}^n$ of $\mathcal{D}(\gamma) = 0$ using well-established algorithms, such as the one described in Ref. [41]. Once the set of roots $\{\gamma_j\}$ has been obtained, we compute β_j as $\beta_j = \sqrt{\gamma_j^2 + k_0^2}$.

As an illustrative example, Table 2 displays the normalized propagation constants β/k_0 for the TM^y modes supported by

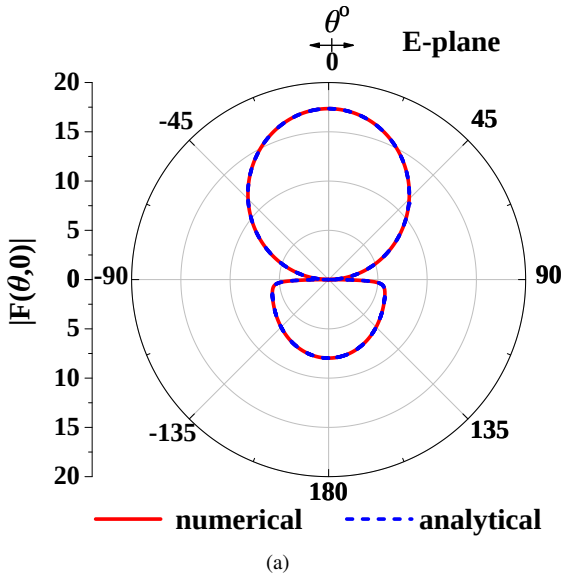

(a)

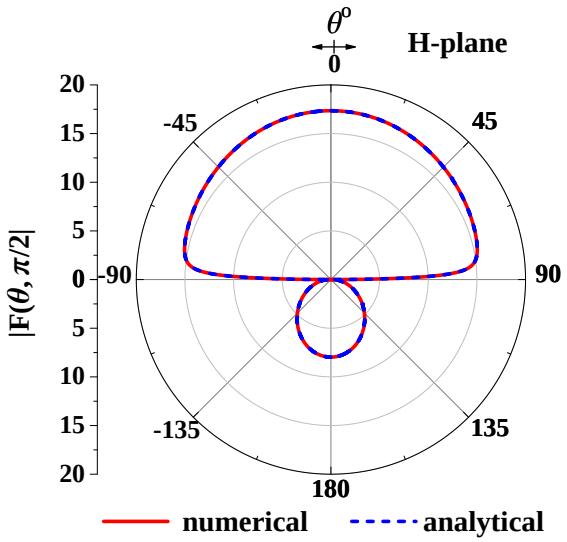

(b)

FIGURE 17. $|\bar{F}(\theta,\varphi)|$**, (a) in the** E**-plane** ($\varphi=0$) **and (b) in the** H**-plane** ($\varphi=\pi/2$) **for** $\bar{p}=1\hat{y}$ **(**Am**),** $k_0=1$**,** $k_0 d=2\pi$**,** $\bar{r}'=(0,0,-d/2)$**,** $\varepsilon_{r1}=\exp(-k_0 z)$**, and** $\mu_{r1}=\exp[k_0(z+d)]$**.**

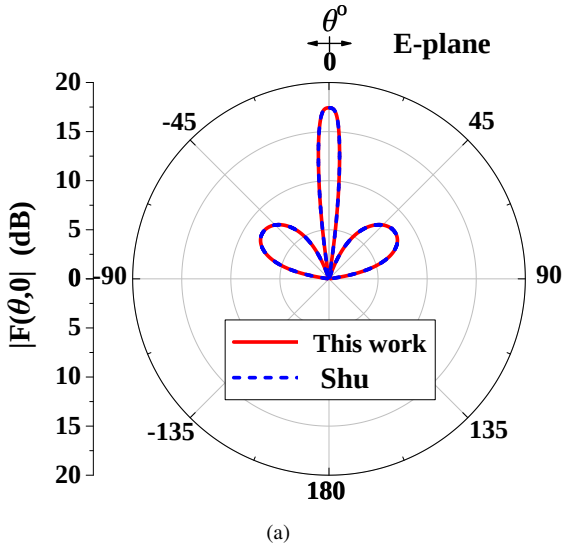

(a)

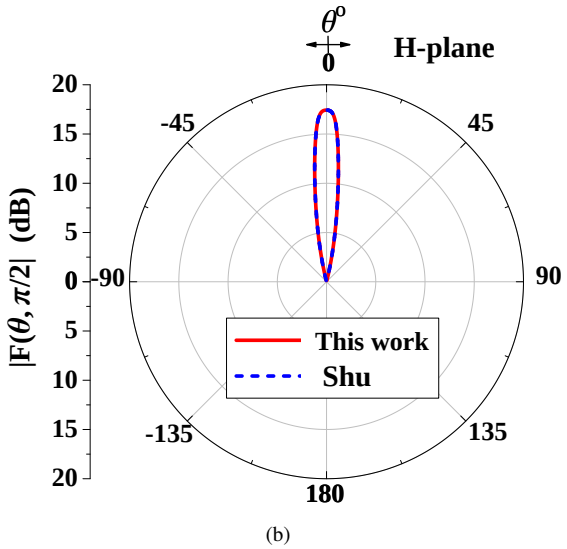

(b)

FIGURE 18. Grounded DNG slab: Radiation pattern $|\bar{F}(\theta,\varphi)|$ **in dB for** $\bar{p}=0.001\hat{x}$ **(**Am**),** $f=5.943$ **GHz,** $d=60$ **mm,** $\bar{r}'=(0,0,0)$**,** $z_0=-d$**,** $z_1=0$**,** $\varepsilon_{r1}=-1.831$**, and** $\mu_{r1}=-0.0238$**. (a)** E**-plane. (b)** H**-plane.**

the bilateral slab of Fig. 2(a). The parameters are as follows: $k_0 d=4\pi$, $\mu_{r1}=1$, and $\varepsilon_{r1}=3+\cos[k_0(z+d)]-i\varepsilon'$ with $\varepsilon'=0$ (representing a lossless dielectric) or $\varepsilon'=0.5$ (indicating a lossy dielectric).

2) Computation of $\mathcal{D}'(\gamma)$ and $w'_{ij}(\gamma)$

Efficient and accurate computation of $\mathcal{D}'(\gamma)$ and its prerequisite, $w'_{ij}(\gamma)$, is a crucial requirement for applying specific root-finding algorithms detailed in Ref. [41]. Additionally, $\mathcal{D}'(\gamma)$ is essential for (99).

We will use the change of variable $z=z(t)$, as defined in (71), and introduce the notations $F(t)=F(t;\gamma)=W_3(z(t),z_0;\gamma)$ and $\Phi(\tau)=\Phi(\tau;\gamma)=A_3(z(\tau);\gamma)$ to emphasize their dependence on the parameter γ. The dependence of $A_3(z)$ on γ becomes evident from (28), where $\gamma_1^2(z)=\gamma^2+k_0^2-\omega^2\varepsilon_1(z)\mu_1(z)$ according to (29). The justification for the dependence of $F(t)$ on γ can be based on (76). Using this notation, we can rephrase (76) as:

$$F(t;\gamma)-\beta\sum_{j=1}^{N}\Phi(t_j;\gamma)F(t_j;\gamma)\sum_{k=0}^{N-1}\frac{w_j}{h_k}P_k(t_j)C_k(t)=I.$$

Upon differentiating with respect to γ, we obtain:

$$\frac{\partial F(t;\gamma)}{\partial\gamma}-\beta\sum_{j=1}^{N}\{\Phi(t_j;\gamma)\frac{\partial F(t_j;\gamma)}{\partial\gamma}+\frac{\partial\Phi(t_j;\gamma)}{\partial\gamma}F(t_j;\gamma)\}\times\sum_{k=0}^{N-1}\frac{w_j}{h_k}P_k(t_j)C_k(t)=0. \quad (100)$$

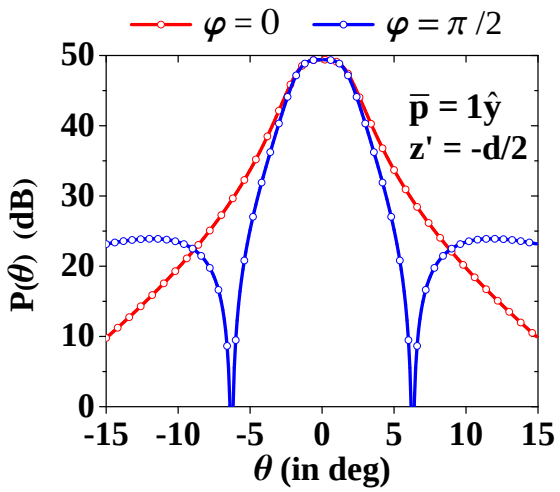

(a)

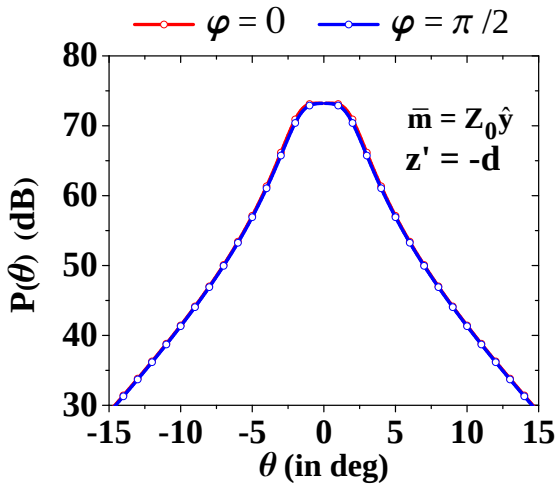

(b)

FIGURE 19. **E-plane and H-plane Power patterns for a μ-near-zero grounded slab at $f = 9.122$ GHz, $d = 75$ mm, $\varepsilon_{r1} = 1.2$, and $\mu_{r1} = 0.01$. (a) Electric dipole $\bar{p} = 1\hat{y}$ (Am) at $\bar{r}' = (0, 0, -d/2)$. (b) Magnetic dipole $\bar{m} = Z_0\hat{y}$ (Vm) at $\bar{r}' = (0, 0, -d)$. Solid lines: this work. Open circles: Ref. [39].**

Applying (100) with $t = t_1, \ldots, t_N$ yields:

$$\frac{\partial F(t_i;\gamma)}{\partial \gamma} - \beta \sum_{j=1}^{N} w_j b_{ij} \Phi(t_j;\gamma) \frac{\partial F(t_j;\gamma)}{\partial \gamma} = \beta \sum_{j=1}^{N} w_j b_{ij} \frac{\partial \Phi(t_j;\gamma)}{\partial \gamma} F(t_j;\gamma), \quad i = 1, \ldots, N, \quad (101)$$

where b_{ij} is given by (79). With $\{F(t_j;\gamma)\}_{j=1}^{N}$ determined from (78), (101) transforms into a linear algebraic system from which we can compute the unknown $\{\partial F(t_j;\gamma)/\partial\gamma\}_{j=1}^{N}$. The required $w'_{ij}(\gamma)$ with $1 \le i, j \le 4$ are the elements of $\partial F(t_N;\gamma)/\partial\gamma$. In terms of them, $\mathcal{D}'(\gamma)$ can be obtained using (95).

TABLE 2. **β/k_0 for an inhomogeneous slab. Parameters: $k_0 d = 4\pi$, $\mu_{r1} = 1$, $\varepsilon_{r1} = 3 + \cos[k_0(z + d)] - i\varepsilon'$ with $\varepsilon' = 0$ and $\varepsilon' = 0.5$.**

	β_i/k_0	
i	$\varepsilon' = 0$	$\varepsilon' = 0.5$
1	1.04804494442525	0.99844346886324 - i 0.137392890929445
2	1.23054600391380	1.23318975167569 - i 0.177503706190931
3	1.45472296058384	1.46344391146134 - i 0.167831444565456
4	1.54923147650879	1.55506026745734 - i 0.152894081358176
5	1.57247500347992	1.57890989681788 - i 0.153761795181344
6	1.80465808008725	1.81116267735049 - i 0.142925345806486

APPENDIX B
EXACT ANALYTICAL SOLUTION FOR SPECIAL CASES

We will focus on the scattering problem in the E-case, noting that the H-case can be addressed through duality. Let

$$\bar{E}_1 = \hat{y} E_{y1}(x, z) = \hat{y} e^{ik_x x} \tilde{E}_{y1}(z).$$

From (5) using (3) and (7), we can derive the generalized Helmholtz equation:

$$\frac{d^2 \tilde{E}_{y1}}{dz^2} - \frac{\mu_1'(z)}{\mu_1(z)} \frac{d\tilde{E}_{y1}}{dz} + (k_1^2(z) - k_x^2)\tilde{E}_{y1} = 0. \quad (102)$$

Here, $k_1^2(z) = \omega^2 \varepsilon_1(z)\mu_1(z)$, and $\mu_1'(z)$ is the derivative of $\mu_1(z)$.

Let $V^+(z)$ and $V^-(z)$ be two linearly independent solutions of (102). Then

$$\tilde{E}_{y1}(z) = c_1 V^+(z) + c_2 V^-(z), \quad (103)$$

where c_1 and c_2 are constant coefficients. In terms of $\tilde{E}_{y1}$, we can obtain $\tilde{H}_{x1}$ from

$$\tilde{H}_{x1} = \frac{1}{i\omega\mu_1} \frac{d\tilde{E}_{y1}}{dz}. \quad (104)$$

By enforcing continuity of both $E_y(z)$ and $H_x(z)$ at the interfaces $z = z_0$ and $z = z_1$, using (2), (3), (103), and (104), we obtain a 4×4 linear system of algebraic equations from which R, T, c_1, and c_2 can be determined.

At this stage, the solution procedure is purely formal because $V^{\pm}(z)$ cannot be expressed in terms of known special functions for general inhomogeneity profiles. In Table 3, we provide a summary of special profiles for which exact solutions to (102) are feasible. The eigen-solutions for Case I to Case VI are presented below.

TABLE 3. **Special inhomogeneity profiles.**

Case	ε_{r1}	μ_{r1}
I	$e^{k_0(d-z)}$	$e^{k_0 z}$
II	$1 + \alpha_1(k_0 z) + \alpha_2(k_0 z)^2$	1
III	$1 + ae^{bz}$	1
IV	1	ae^{bz}
V	$a + \cos(bz)$	1
VI	$\frac{b}{1+az}$	$1 + az$

Case I: $V^{\pm}(z) = e^{\frac{z}{2}(k_0 \pm \sqrt{k_0^2 + 4{k_x}^2 - 4e^{k_0 d} {k_0}^2})}$.

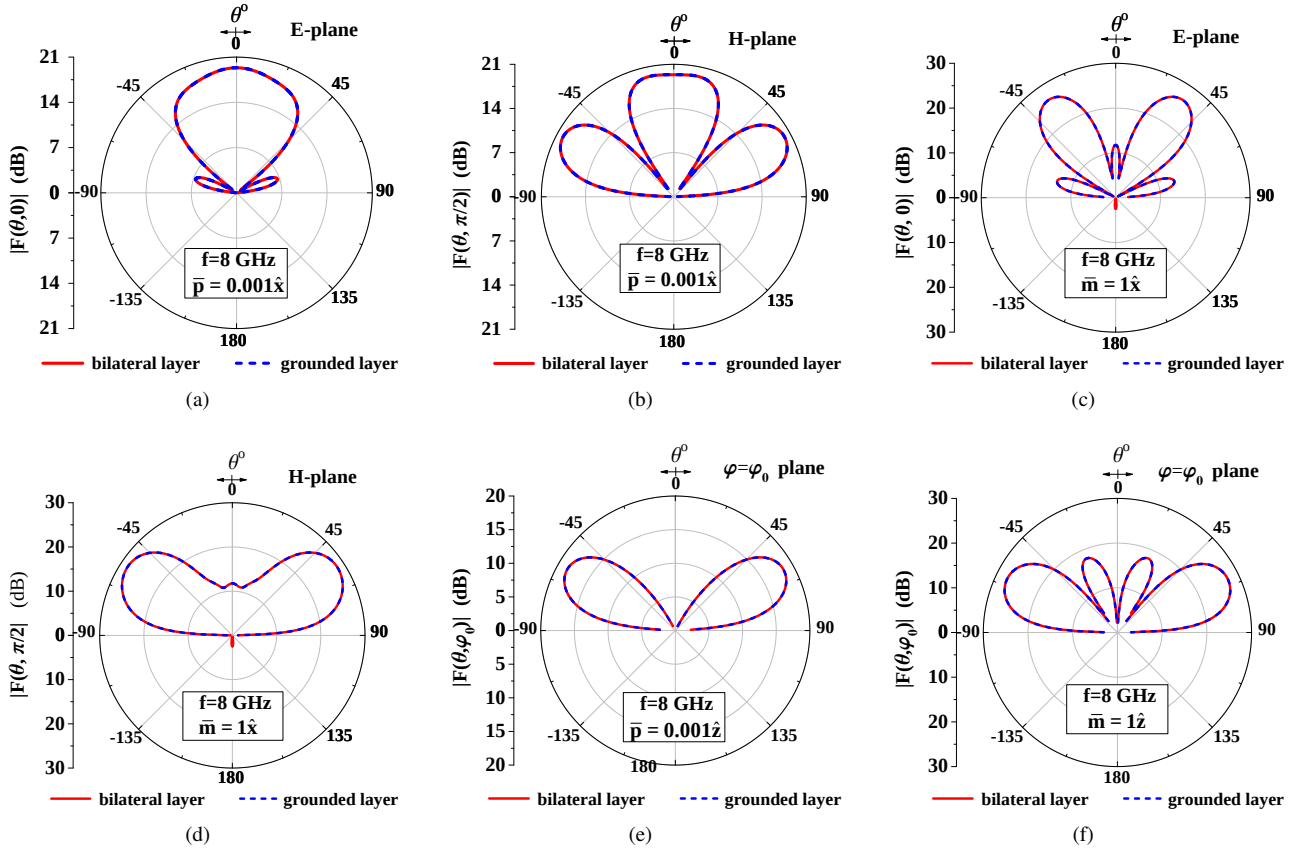

FIGURE 20. **Radiation patterns $|\bar{F}(\theta,\varphi)|$ in dB for electric and magnetic dipoles at $\bar{r}'=(0,0,0)$ with $d=10$ cm, $\alpha=1$, $\nu_0=1$ GHz, $n_0=10^{18}$ m^{-3}, $f=8$ GHz. Solid lines: bilateral plasma layer, dotted lines: grounded plasma layer.**

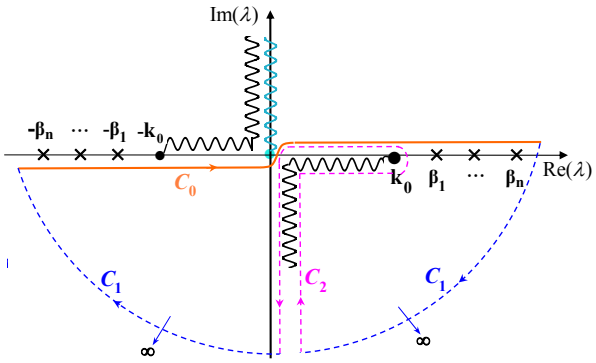

FIGURE 21. **Path of integration in the complex $\lambda-$ plane.**

Case II: $V^{\pm}(z)=D_{\nu^{\pm}}[g^{\pm}(z)]$,
where $D_\nu(z)$ is the parabolic cylinder function, and:

$$g^{\pm}(z)=\frac{\pm 1+i}{2{\alpha_2}^{3/4}}(\alpha_1+2k_0\alpha_2 z),$$

$$\nu^{\pm}=\frac{\pm i}{8{k_0}^2{\alpha_2}^{3/2}}\left[(\pm 4i{\alpha_2}^{3/2}-4\alpha_2+{\alpha_1}^2){k_0}^2+4{k_x}^2\alpha_2\right].$$

Case III: $V^{\pm}(z)=J_{\pm\frac{2ik_z}{b}}\left(2k_0\sqrt{ae^{bz}}/b\right)$,
where $J_\lambda(\cdot)$ denotes the Bessel function of the first kind.
Case IV: $V^{\pm}(z)=e^{\frac{bz}{2}}J_{\pm\frac{\sqrt{b^2+4{k_x}^2}}{b}}\left(2k_0\sqrt{ae^{bz}}/b\right)$.

Case V:

$$V^{\pm}(z)=\texttt{Mathieu}_S^C\left[-\frac{4}{b^2}\left({k_x}^2-a{k_0}^2\right),-\frac{2{k_0}^2}{b^2},\frac{bz}{2}\right].$$

Here $\texttt{MathieuC}[a,q,z]/\texttt{MathieuS}[a,q,z]$ denote the even/odd Mathieu function with characteristic value a and parameter q. The Mathieu functions are solutions to the equation $y''+[a-2q\cos(2z)]y=0$.

Case VI:

$$V^{+}(z)=u(z)J_1[\upsilon(z)],\quad V^{-}(z)=u(z)Y_1[\upsilon(z)],$$

where Y_1 denotes the Bessel function of the second kind, and

$$u(z)=\sqrt{1+az}\{q(z)\}^{1/2},\quad \upsilon(z)=-\frac{i}{a}q(z)$$

with $q(z)=az\sqrt{{k_x}^2-b{k_0}^2}+i\sqrt{b{k_0}^2-{k_x}^2}$.

For additional inhomogeneity profiles with exact solutions to the wave equation, see Section 4.3.4 in Ref. [29].

ACKNOWLEDGMENT

The publication of the article in OA mode was financially supported by HEAL-Link.

REFERENCES

[1] A. Toscano, L. Vegni, and F. Bilotti, "A new efficient method of analysis for inhomogeneous media shields and filters," *IEEE Trans. Electromagn. Compat.*, vol. 43, no. 3, pp. 394–399, 2001.

[2] F. Bilotti, A. Toscano, and L. Vegni, "Design of inhomogeneous slabs for filtering applications via closed form solutions of the reflection coefficient," *J. Electromagn. Waves Appl.*, vol. 16, no. 9, pp. 1233–1254, 2002.

[3] M. Khalaj-Amirhosseini, "Wideband flat radomes using inhomogeneous planar layers," *Int. J. Antennas Propag.*, vol. 2008, pp. 1–6, 2008.

[4] M. Chamanzar, K. Mehrany, and B. Rashidian, "Legendre polynomial expansion for analysis of linear one-dimensional inhomogeneous optical structures and photonic crystals," *J. Opt. Soc. Am. B: Opt. Phys.*, vol. 23, no. 5, pp. 969–977, 2006.

[5] A. E. Serebryannikov and K. Schuenemann, "Reflections from almost-periodic graded anisotropic slabs," *Microw. Opt. Technol. Lett.*, vol. 48, no. 7, pp. 1320–1324, 2006.

[6] A. E. Serebryannikov, O. Y. Vasylchenko, and A. L. Teplyuk, "Study of band gaps in transmission spectrum of 1D inhomogeneous slab with almost periodic continuous permittivity profile," *Microw. Opt. Technol. Lett.*, vol. 46, no. 2, pp. 134–139, 2005.

[7] C. Gurel and E. Oncu, "Interaction of electromagnetic wave and plasma slab with partially linear and sinusoidal electron density profile," *Prog. Electromagn. Res. Lett.*, vol. 12, pp. 171–181, 2009.

[8] P. Yeh, *Optical Waves in Layered Media.* Wiley, 1988.

[9] I. Abdulhalim, "Analytic propagation matrix method for linear optics of arbitrary biaxial layered media," *J. Opt. A: Pure Appl. Opt.*, vol. 1, no. 5, pp. 646–653, 1999.

[10] Z. Lu, "Accurate calculation of reflectance spectra for thick one-dimensional inhomogeneous optical structures and media: stable propagation matrix method," *Opt. Lett.*, vol. 33, no. 17, pp. 1948–1950, 2008.

[11] D. Zarifi, M. Soleimani, and A. Abdolali, "State transition matrix of inhomogeneous planar layers," *IET Microw. Antennas Propag.*, vol. 9, no. 4, pp. 301–306, 2015.

[12] W. C. Chew, *Waves and Fields in Inhomogeneous Media*, ser. IEEE Press series on electromagnetic waves. New York: IEEE Press, 1995.

[13] T. Cui and C. Liang, "Nonlinear differential equation for the reflection coefficient of a pure conducting medium and its novel inverse scattering solution," *IEEE Trans. Geosci. Remote Sens.*, vol. 32, no. 3, pp. 709–712, 1994.

[14] M. Khalaj-Amirhosseini, "Analysis of lossy inhomogeneous planar layers using Taylor's series expansion," *IEEE Trans. Antennas Propag.*, vol. 54, no. 1, pp. 130–135, 2006.

[15] ——, "Analysis of lossy inhomogeneous planar layers using Fourier series expansion," *IEEE Trans. Antennas Propag.*, vol. 55, no. 2, pp. 489–493, 2007.

[16] S. E. Hosseininejad, A. Abdolali, and N. Komjani, "Radiation and scattering from a point source on an inhomogeneous substrate," *IET Microw. Antennas Propag.*, vol. 8, no. 15, pp. 1327–1332, 2014.

[17] T. Magath and A. E. Serebryannikov, "Fast iterative, coupled-integral-equation technique for inhomogeneous profiled and periodic slabs," *J. Opt. Soc. Am. A Opt. Image Sci. Vis.*, vol. 22, no. 11, pp. 2405–2418, 2005.

[18] E. Soltanmoradi, B. Shokri, and V. Siahpoush, "Study of electromagnetic wave scattering from an inhomogeneous plasma layer using Green's function volume integral equation method," *Phys. Plasmas*, vol. 23, no. 3, p. 33304, 2016.

[19] V. S. Serov, H. W. Schürmann, and E. Svetogorova, "Integral equation approach to reflection and transmission of a plane TE-wave at a (linear/nonlinear) dielectric film with spatially varying permittivity," *J. Phys. A: Math. Theor.*, vol. 37, no. 10, pp. 3489–3500, 2004.

[20] A. Rostami and H. Motavalli, "Asymptotic iteration method: A powerful approach for analysis of inhomogeneous dielectric slab waveguides," *Prog. Electromagn. Res. B*, vol. 4, pp. 171–182, 01 2008.

[21] K. Kim, D.-H. Lee, and H. Lim, "Theory of the propagation of coupled waves in arbitrarily inhomogeneous stratified media," *EPL*, vol. 69, no. 2, pp. 207–213, 2005.

[22] A. Ghaffar, A. Hussain, Q. A. Naqvi, and K. Hongo, "Radiation characteristics of an inhomogeneous slab using Maslov's method," *J. Electromagn. Waves Appl.*, vol. 22, no. 2-3, pp. 301–312, 2008.

[23] E. A. Hashish, "Forward and inverse scattering from an inhomogeneous dielectric slab," *J. Electromagn. Waves Appl.*, vol. 17, no. 5, pp. 719–736, 2003.

[24] T. Gric and M. Cada, "Analytic solution to field distribution in one-dimensional inhomogeneous media," *Opt. Commun.*, vol. 322, pp. 183–187, 2014.

[25] S. G. Krivoshlykov, *Quantum-Theoretical Formalism for Inhomogeneous Graded-Index Waveguides*. Berlin: Akademie Verlag, 1994.

[26] J. L. Tsalamengas, "Oblique scattering from radially inhomogeneous dielectric cylinders: An exact Volterra integral equation formulation," *J. Quant. Spectrosc. Radiat. Transf.*, vol. 213, pp. 62–73, 2018.

[27] ——, "Oblique scattering from radially inhomogeneous bianisotropic cylindrical structures analyzed using a highly accurate Volterra integral equation approach," *IEEE Trans. Antennas Propag.*, vol. 69, no. 11, pp. 7811–7819, 2021.

[28] ——, "Spectrally-accurate analysis of EM scattering by material and metamaterial, isotropic or anisotropic, radially inhomogeneous spherical objects," *IEEE Trans. Antennas Propag.*, vol. 70, no. 8, pp. 6934–6943, 2022.

[29] G. Tyras, *Radiation and Propagation of Electromagnetic Waves*. Academic Press New York; Sydney, 1969.

[30] A. Nosich, "Radiation conditions, limiting absorption principle, and general relations in open waveguide scattering," *J. Electromagn. Waves Appl.*, vol. 8, no. 3, pp. 329–353, 1994.

[31] S. Brueck, "Radiation from a dipole embedded in a dielectric slab," *IEEE J. Sel.Top. Quantum. Electron.*, vol. 6, no. 6, pp. 899–910, 2000.

[32] N. L. Tsitsas, C. Valagiannopoulos, and A. I. Nosich, "Excitation of guided waves on a lossless dielectric slab by an E-polarized complex source point beam," *IEEE Trans. Antennas Propag.*, vol. 67, pp. 5532–5543, 2019.

[33] A. Kirsch and A. Lechleiter, "The limiting absorption principle and a radiation condition for the scattering by a periodic layer," *SIAM J. Math. Anal.*, vol. 50, no. 3, pp. 2536–2565, 2018.

[34] R. E. Collin and F. J. Zucker, *Antenna theory (Ch. 3)*. McGraw-Hill, 1969.

[35] J. Shen, T. Tang, and L.-L. Wang, *Spectral Methods: Algorithms, Analysis and Applications*, 1st ed. Berlin, Heidelberg: Springer Berlin Heidelberg, 2011.

[36] T. Tang, X. Xu, and J. Cheng, "On spectral methods for Volterra type integral equations and the convergence analysis," *J. Comput. Math.*, vol. 26, pp. 825–837, 2008.

[37] D. C. Tzarouchis and A. Sihvola, "Polarizability of radially inhomogeneous subwavelength spheres," *Phys. Rev. Appl.*, vol. 10, p. 054012, Nov 2018.

[38] W. Shu, "Electromagnetic waves in double negative metamaterials and study on numerical resonances in the method of moments (MoM)," PhD dissertation, Iowa State University, 2008.

[39] G. Lovat, P. Burghignoli, F. Capolino, and D. R. Jackson, "Combinations of low/high permittivity and/or permeability substrates for highly directive planar metamaterial antennas," *IET Microw. Antennas Propag.*, vol. 1, pp. 177–183, February 2007.

[40] V. O. Byelobrov and A. Nosich, "Mathematical analysis of the lasing eigenvalue problem for the optical modes in a layered dielectric cavity with a quantum well and distributed Bragg reflectors," *Opt. Quantum Electron.*, vol. 39, pp. 927–937, 2007.

[41] L. M. Delves and J. N. Lyness, "A numerical method for locating the zeros of an analytic function," *Math. Comput.*, vol. 21, no. 100, pp. 543–560, 1967.

JOHN L. TSALAMENGAS received the diploma degree in Electrical and Mechanical Engineering and the doctor's degree in Electrical Engineering from the National Technical University of Athens (NTUA), Athens, Greece, in 1977 and 1983, respectively.

In 1984, he joined NTUA, where he was a Professor of electrical engineering since 1995 until his retirement (as a Professor Emeritus of NTUA) in September 2020. He coauthored (with Prof. J. A. Roumeliotis) a two-volume book on EM fields and waves, in Greek. His research interests include computational and applied electromagnetics, numerical analysis, and applied mathematics.